Development of Color Ratio Thin Filament Pyrometry Approach for Applications in High Speed Flames

Kai A. Hagmann

Thesis submitted to the faculty of the Virginia Polytechnic Institute and State University in partial fulfillment of the requirements for the degree of

Master of Science
In
Aerospace Engineering

Joseph Meadows

Todd Lowe

Gregory Young

May 4th, 2023
Blacksburg, VA

Keywords:

Thin filament pyrometry, graybody radiation, flame temperature, flat flame burner

Development of Color Ratio Thin Filament Pyrometry Approach for Applications in High Speed Flames

Kai A. Hagmann

ABSTRACT

Thin filament pyrometry is a proven technique used to measure flame temperature by capturing the spectral radiance produced by the immersion of silicon carbide filaments in a hot gas environment. In this study a commercially available CMOS color camera was used, and the spectral response of each color channel was integrated with respect to the assumed graybody radiation spectrum to form a look up table between color ratio and temperature. Interpolated filament temperatures are then corrected for radiation losses via an energy balance to determine the flame temperature. Verification of the technique was performed on the Holthuis and Associates Flat Flame Burner, formerly known as the Mckenna Burner, and the results are directly compared to literature values measured on a similar burner. The results are also supported by radiation corrected measurements taken using a type B thermocouple on the same burner setup. An error propagation analysis was performed to determine which factors contribute the most to the final measurement uncertainty and confidence intervals are calculated for the results. Uncertainty values for a single point measurement were determined to be between ±15 and ±50 K depending on the color ratio and the total uncertainty associated with day-to-day changes in the measurement setup was found to be ±55 K.

Development of Color Ratio Thin Filament Pyrometry Approach for Applications in High Speed Flames

Kai A. Hagmann

GENERAL AUDIENCE ABSTRACT

Determination of flame temperature is an important aspect of combustion research and is often critical to the evaluation of combustion systems as well as the integration of those systems into more complex devices. In this thesis the technique of thin filament pyrometry was implemented and verified through the use of a well characterized calibration flame. This technique involves placing thin filaments usually made from silicon carbide into the flame and capturing the spectrum of light they emit with a detector. Since the amount of light emitted as well as which wavelengths the light is concentrated in is a strong function of temperature, this methodology may be used to calculate the temperature of the flame. Thin filament pyrometry has the advantage compared to other techniques in that it is extremely cheap to implement and requires no advanced scientific equipment. The SiC filaments have been shown to have a very high resistance to the flame environment and do not face many of the same challenges that can cause problems for other techniques. A statistical analysis of the method implemented in this work was also performed and the expected uncertainty was similar to many of the alternative techniques which necessitate a more complex or expensive setup.

Dedication

To my family and friends for always having my back.

Acknowledgements

I would like to thank my entire committee, Dr. Joseph Meadows, Dr. Todd Lowe, and Dr. Gregory Young for their support and guidance through the development of this thesis. I would also like to thank Dr. Meadows specifically for demanding excellence and by that virtue teaching me to demand it from myself. His guidance, advice, and wealth of knowledge were invaluable to the completion of this work.

I would also like to thank the members of my research group, Yogesh Aradhey, Shrikar Banagiri, Keaton Hanley, Ashwin Kumar, Piyush Raj, and Dharmik Rathod for their continued support when it came to testing support, brain storming, or helping me figure out the many problems I encountered over the course of this work.

I would also like to thank the staff of the Advanced Propulsion and Power Laboratory, machinist Randall Monk, and lab manager Jason Doby, for their work and dedication and for always lending a hand when needed.

Table of Contents

List of Figures

List of Abbreviations

CARS	Coherent Anti-Stokes Raman Scattering
CMOS	Complementary Metal–Oxide–Semiconductor
DSLR	Digital Single-Lens Reflex
TFP	Thin Filament Pyrometry
PID	Piping and Instrumentation Diagram
MFC	Mass Flow Controller
ISO	International Organization for Standardization
DLR	Deutsches Zentrum für Luft- und Raumfahrt
SCFH	Standard Cubic Feet per Hour
SLPM	Standard Liters Per Minute

Chapter 1. Introduction

1.1 Motivation

Throughout the years having an accurate method for determining the temperature of a flame has been an essential component to meaningful research in the field of combustion and many closely related disciplines. This is first and foremost due to the fact that flame temperature is fundamentally related to many other key quantities of interest including but not limited to species concentrations, equivalence ratio, and flame propagation speed. Also, concerning the implementation of combustion devices, temperature is critical when it comes to the design of other important components such as turbine assemblies in the case of a jet engine or facility exhaust systems in the case of a gas turbine power plant. For either situation, proper measurement of the expected temperatures is necessary in order for adequate sizing and materials selection to be performed. Determination of temperature also allows for novel combustion systems or regimes to be characterized when it comes to the effects of fuel type, mixing, atomization, vaporization, anchoring, etc. Without an appropriate and precise measurement of temperature in any of these cases, the comparison and independent analysis of other variables becomes much more difficult.

The first method ever used to conduct temperature measurements was the thermometer, a device which utilizes the expansion of a fluid in a tube, nominally either mercury or alcohol, to indicate the temperature of the fluid. This was surpassed by the thermocouple, invented in 1821 by Thomas Seebeck, which utilizes two wires of different thermal and electrical conductivities junctioned together at one end and connected to a voltage measurement device at the other (Hunt & Matthey, 1964). When the junction is placed in a hot medium, a temperature gradient and, as a result, a gradient of free electrons is induced in each wire depending on its respective thermal and electrical conductivities. This can be measured as a voltage difference between the two wires which, through a calibration procedure using known temperature sources, can be correlated to the temperature of the junction. However, both of these methods have some key drawbacks. Thermometer measurement is moot for combustion applications as the boiling point of any practical fluid is far below the temperature of any flame that would be measured. Thermocouple measurement however has a fairly extensive history of application when it comes to combustion and is often the standard in many laboratory environments. Many different types or classes of thermocouples exist constructed from different metals which are suitable for different ranges of temperature measurement. This is based on the Seebeck coefficient or the ratio between the induced thermoelectric voltage and the temperature gradient across the alloy in question. For a thermocouple to have good precision over a certain range of temperatures both metals or alloys being used must have either a constant or well characterized Seebeck coefficient over that range. However, since many environmental factors such as oxidation can affect the coefficient, thermocouples designed for high temperature applications often necessitate the use of chemically inert materials such as latinum, which is both expensive as well as a conflict resource (Butler et al., 2003). Lastly, both thermometers and thermocouples suffer when it comes to combustion applications in that they are restricted to generating a measurement at a single point in the flow field. They are also often intrusive geometrically speaking to the point where they can alter the flow field itself and must be corrected for radiation losses etc. to obtain an accurate gas phase temperature measurement.

The second, or newer generation of flow temperature measurement techniques can be categorized as being generally optics based and uses the spectral radiance or luminescence of either the flame itself or an emitter placed in the flow field to infer temperature. In many cases these techniques rely on either the emission or absorption bands of a certain species found in the flame and capture either their natural or laser exited radiance to infer temperature. Some notable examples include N_2 coherent anti-Stokes Raman scattering (CARS) which utilizes the vibrational states and transitions of the exited N_2 molecules as well as OH* based methodologies which interpret the higher concentrations in areas of heat release to determine temperature. However, while both of these methods are capable of delivering either single point temperature measurements or two-dimensional profiles via inverse Abel transformation, there are several drawbacks. Namely, many of these techniques often necessitate the use of strictly characterized scientific grade emitters, lasers, detectors, and other optical systems. The temperature measurement generated is then directly dependent on the accuracy, calibration, and noise properties of these instruments. Additionally, the upfront cost is quite significant for the implementation of many of these techniques creating a barrier of sorts to their use. Another technique of note, thin filament pyrometry (TFP), which is the method that was implemented in this work, utilizes the spectral radiance of a body placed in the flame captured via a detector to calculate temperature. This method is usually predicated on the assumption that the distribution of spectral radiance of the body can be assumed to be that of a graybody and the spectral response of the detector or imaging system is well characterized. The body placed in the flame, normally a thin filament as the name would suggest, must also be sufficiently small such that it does not significantly disrupt the flow field and adversely impact the measurement.

Thin filament pyrometry has several distinct advantages when compared to the other measurement techniques discussed to this point. First, it is capable of delivering temperature profiles along the length of the filament, the geometric precision of which is solely determined by the imaging system in use. Second, when sized correctly it induces minimal disruptions to the flow field being measured and requires very few complex error inducing post processing techniques to yield temperature measurements. Third, the threshold in terms of cost of implementation is relatively low and it has been demonstrated successfully with even the most basic consumer grade digital cameras being used as the detection system. Finally, TFP is not dependent whatsoever on the chemical composition or scale of the flame in question having been proven effective in low Reynolds number diffusion flames and in high pressure near-sonic speed flows alike. This last fact is of particular note when it comes to the goals of our research group as a whole where the development of a single technique capable of delivering accurate measurements across a variety of combustion environments is particularly desirable. It is the goal that through the implementation and characterization of this technique, this work will provide a relatively simple and cost-effective methodology that can support a variety of research goals in the years to come.

1.2 Thesis Contributions

The objectives of this work were twofold - to evaluate the performance of the thin filament pyrometry technique employing a CMOS color camera as the detector and to analyze the uncertainties introduced to the final temperature results through various components of the setup and processing techniques. The accuracy of the technique was analyzed through the use of a well

characterized flame source and compared to experimental results found in the literature. Influences of the camera setup including lens throughput, aperture, proper focus, and exposure time as well as the transmission curves of any filters were analyzed as well as categorized with regards to impact. A methodology for determining the error of the measurements performed as well as any future measurements was developed accounting for any uncertainties due to flow measurement/control devices, camera and filter response, interpolation of temperature from color ratios, correlations and assumptions with regards to radiation correction, and the influence of image population.

1.3 Document Overview

In Chapter 2 a comprehensive review of current and past literature surrounding the thin filament pyrometry technique will be presented covering a timeline beginning with the first successful implementation in 1988 all the way through more recent developments and innovations. Key differences between different approaches will be discussed with emphasis placed on how they impacted the final result and accuracy. Approaches that yielded major breakthroughs with respect to either accuracy or precision or those with either setup or applications which most closely follow this work will be the subject of further discussion. In Chapter 3 the underlying equations and mathematical processes that govern thin filament pyrometry will be detailed and explained. Chapter 4 will discuss the hardware implementation and setup including the flame itself, all flow control devices, the camera and filter configuration, and the verification of each of these components. The post processing and software implementation will be discussed in Chapter 5 detailing the methods that were used to convert the raw images to the final temperature result. In this section there will also be some discussion as to how each component independently contributes to the net error of the final result. In Chapter 6 the results of this work will be presented and compared with both literature and other sources of data. Finally, in Chapter 7 the conclusions of the work will be stated and possible targets or implementations for future work will be proposed and discussed in detail.

Chapter 2. Literature Review

The first successful implementation of thin filament pyrometry was performed by Vilimpoc et al., 1988 and used 15 μm β-SiC filaments placed in both hydrogen-air diffusion and propane-air premixed flames to develop the technique. An InGaAs diode detector was used in conjunction with a rotating mirror to image the filament in the flame from left to right leading to an estimated spatial resolution of 120 μm per sample point. This first formulation of the technique has now come to be known as intensity ratio pyrometry and would become the dominant variety in the years to come. In this method, a calibration point is first generated by imaging the filament in a flame of known temperature. If the spectral response of the detector is known, then a look up table can be created by taking the ratio of the integrated graybody spectrum at the calibration temperature and the temperature of interest. From this point a radiation correction is used to determine the temperature of the gas phase from the temperature of the filament. The study estimated the temporal response of the filament to be on the order of 750 Hz which was attributed to its low thermal conductivity. The uncertainty was estimated to be ±80 K for a reading of 1100 K but only ±8K for a measurement in the range of 2300 K. The measurements of flame temperature matched the theoretical adiabatic flame temperature to within 5 K. Temporal readings were also taken and were used to estimate the periodic frequency of the buoyancy driven vortices in the diffusion flame.

Another implementation of intensity ratio pyrometry was performed by Maun et al., 2007 where similar filaments were placed in a coflowing methane-air laminar jet diffusion flame and imaged using a Nikon D100 consumer-grade 6 megapixel camera. The methodology for calculating temperature was essentially unchanged and the calibration point was verified using a type B thermocouple. A Schott BG-26 colored glass filter was employed to balance the radiation spectrum and intensity values were extracted as the average of a 5 pixel band around the filament. The effects of soot deposition and aging were examined by placing filaments at different heights in the flame and monitoring the intensity over time. Soot deposition was found to be extremely problematic for thermocouple measurements especially in certain regions but had less of an effect on the filament derived temperatures. This implementation was stated as being capable of measuring gas temperatures in the range of 1400-2200 K and had an estimated uncertainty of ±60 K. The precision of the temperature measurement was determined to be ±0.215 K while the spatial and temporal resolutions were 42 μm and 0.66 ms respectively.

The first implementation of color ratio pyrometry was performed by Kuhn et al., 2011 utilizing two consumer grade DSLR color cameras being the Nikon D70 and D90. This technique was a major advancement as with the color ratio method no calibration point was needed. The spectral response of each color channel for both cameras was verified through the use of a calibrated illumination source and an imaging spectrograph. With this in place, color ratios could be calculated by integrating each color channel response in conjunction with the graybody radiation spectrum. A blackbody source was also used to verify the calculated color ratios versus temperature. Measurements were made in an axisymmetric laminar ethylene diffusion flame which was diluted to varying degrees with nitrogen to alter the flame temperature. Filaments were placed at four different heights within the flame and the processed temperature results showed good agreement with calculated values. The maximum variation between the temperatures derived from the three ratios was around 20 K and could be assumed to be accurate above 1400 K. Intensity values also reached a stable condition after only three minutes of aging in the flame.

A study comparing the techniques of intensity ratio and color ratio pyrometry was conducted by Ma et al., 2013 utilizing a Nikon D300s as the detector along with a Schott BG-7 colored glass filter. Detailed aging tests of 90 minutes each were performed for four different types of SiC filaments via the use of a spectrometer. Two types of filaments, CG-Nicalon and SCS-9A, were found to be stable showing a maximum signal variation of 5% before reaching a steady value. The other two filaments were determined to be unstable and never reached a steady value. The spectral emissivity of the two stable fibers was also measured and was found to be constant with a margin of error across wavelengths between 450 and 700 nm. Accuracy tests were performed through the use of a methane-air premixed flat flame at a height of 3 cm above the burner plug. Fiber derived temperature measurements were shown to have excellent agreement with CARS measurements performed on the same burner. An error propagation analysis was also performed which estimated the temperature measurement uncertainty to be ±36 K and ±45 K for the intensity and color ratio approaches respectively.

In 2013 Dunn-Rankin et al. performed color ratio pyrometry using a Nikon D90 digital camera to determine the temperature of both methane hydrate and counterflow non-premixed water laden methane-air flames. The camera was first calibrated using a blackbody furnace at temperatures between 750 and 1700 C to verify the spectral response. Images were taken of filaments in both flames and the R/G color ratio was used to determine temperature. The temperatures showed acceptable agreement with thermocouple measurements with a maximum deviation of around 90 K. The uncertainty of the measurements was estimated to be ±40 K. A similar study was performed by Sun et al., 2021 on a butane-air premixed Bunsen burner flame. A high-precision Dhyana 400BSI V2 sCMOS camera was used to capture images of the filaments and was also calibrated through the use of a tungsten-rhenium filament. Measurements were also performed using a type K thermocouple which showed a maximum deviation of 5% compared to the filament derived temperatures.

Intensity ratio pyrometry was revisited by Wang et al., 2014 utilizing a near infrared camera to perform temperature measurements at the exit plane of an atmospheric combustion rig burning Jet-A. The rig featured an exhaust Mach number of 0.38 making it the highest speed application of TFP to date. Two dimensional temperature maps were obtained for different global equivalence ratios using radiation corrected type B thermocouple measurements as a calibration point. A statistical analysis of the radiation correction procedure yielded an uncertainty of the measured gas phase temperature of ±55 K. However, by the same analysis it was determined that the uncertainty could be reduced to below ±50 K at higher pressures or exit Mach numbers. This conclusion in particular shows potential for the future of the thin filament pyrometry technique as many other methods of temperature measurement struggle in these kinds of environments.

Chapter 3. Background and Methodology

3.1 Color Ratio Calculation

As mentioned previously, this work focused on the implementation of color-ratio thin filament pyrometry to determine the filament surface temperature, and, via radiation correction, the gas phase temperature. This methodology has a distinct advantage compared to the intensity-ratio approach in that it does not require a calibration point at a known temperature to determine all other temperatures measured on the same flame. As a result, the technique will be more widely applicable, and less effort is required whenever the setup or flame is changed. In this work a complementary metal–oxide–semiconductor (CMOS) sensor type commercially available color camera was used, namely the FASTCAM NOVA S16 by Photron. Additionally, all images were taken through an AF Micro-Nikkor 60mm f/2.8D lens. Since an accurate characterization of the camera's relative spectral response for each color channel is essential for this technique, this information was sourced directly from the manufacturer. The relative spectral response of the camera alone is shown in Figure 1.

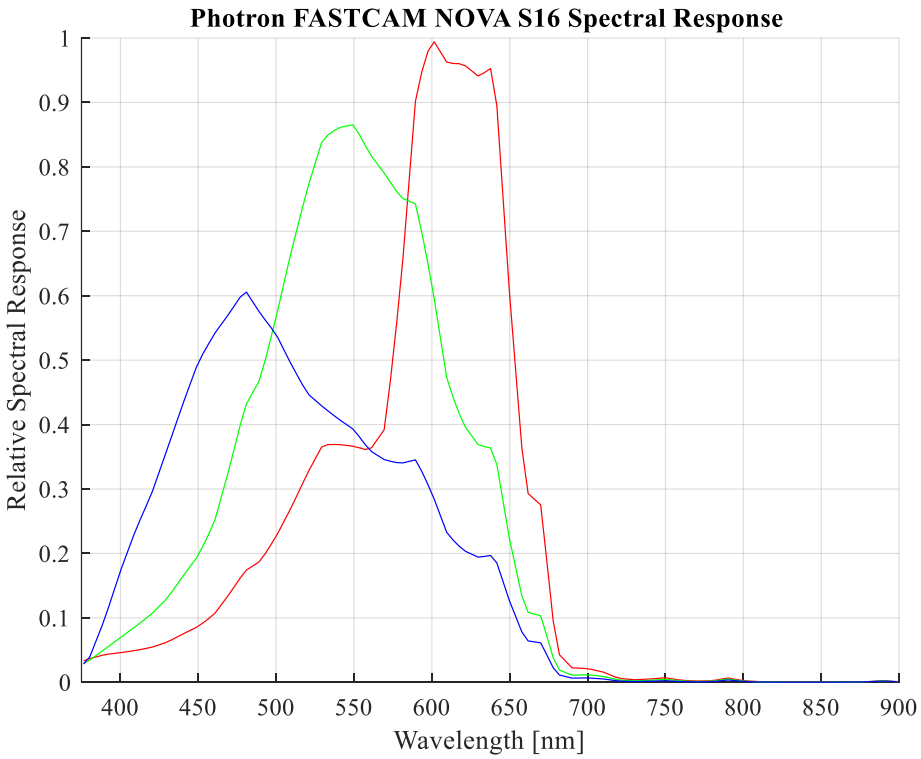

Figure 1: Photron FASTCAM NOVA S16 spectral response for each color channel.

The lens itself also has some internal transmittance curve which is shown below in Figure 2.

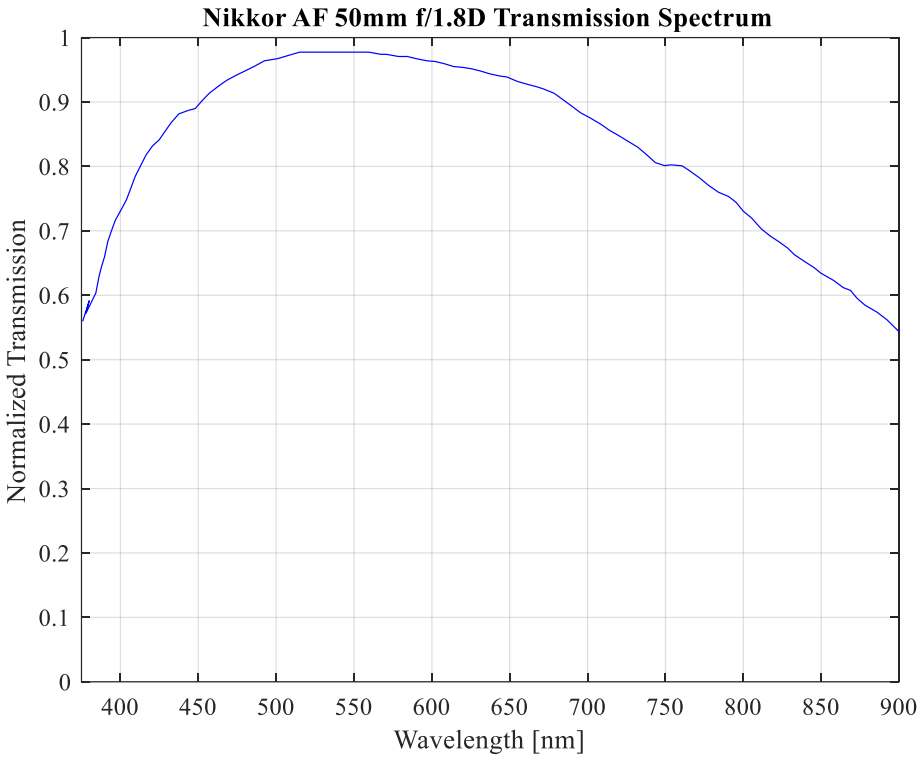

Figure 2: AF Micro-Nikkor 60mm f/2.8D internal transmission spectrum.

In addition, a color glass filter was used in order to balance the intensity seen between the three color channels and as a result achieve a better signal to noise ratio overall. For this work a 50x50x1mm SCHOTT BG-7 filter manufactured by Edmunds Optics was selected, the transmission spectrum for which is shown in Figure 3.

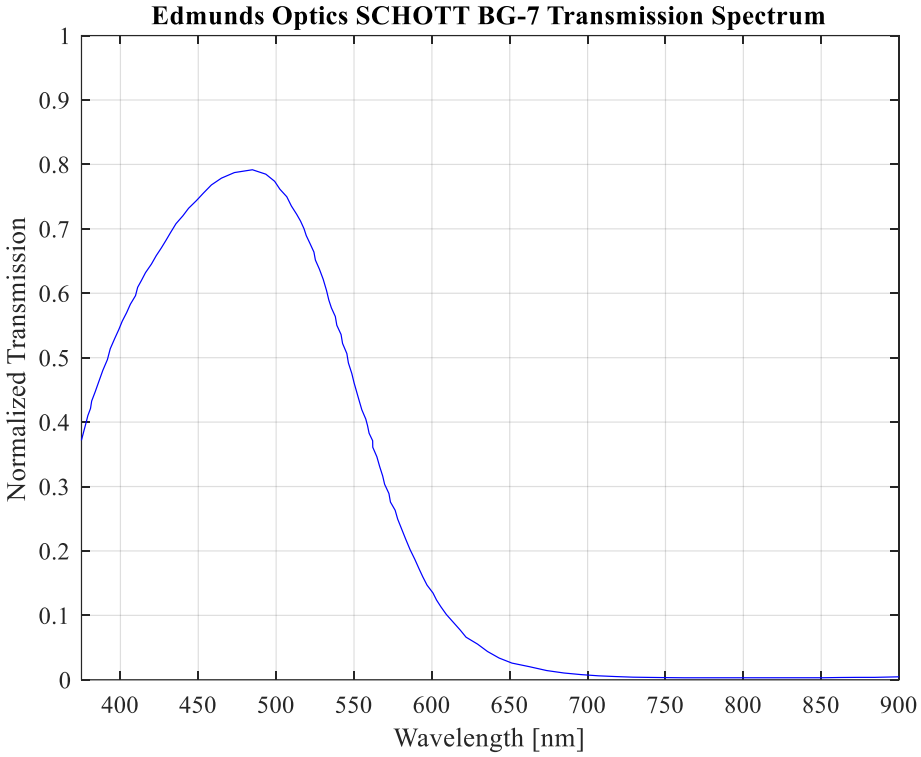

Figure 3: Edmunds Optics SCHOTT BG-7 filter transmission spectrum.

This filter has a drastic impact on the effective spectral response seen by the camera. As can be seen in Figure 4, the red channel in particular is reduced the most which makes sense since this will be the first channel that is saturated by a graybody radiation spectrum.

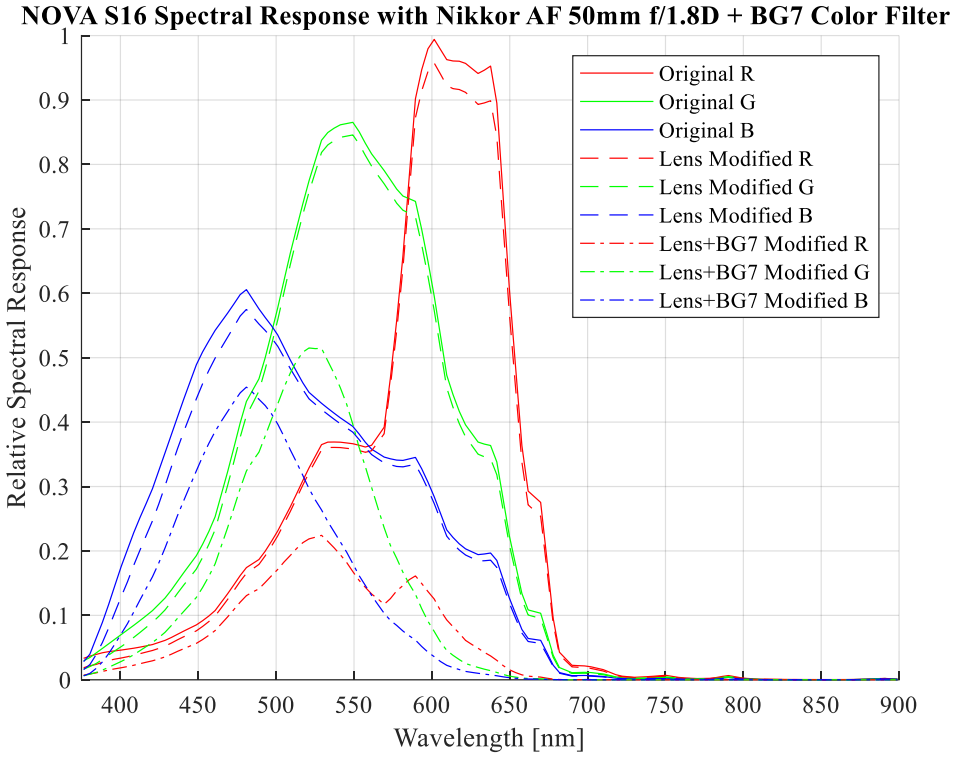

Figure 4: Effective camera spectral response with both lens and color glass filter.

The typical graybody radiation distribution is described by Plank's Law and is given by Eq.1 as

$$B_\lambda(\lambda, T) = \varepsilon \frac{2hc^2}{\lambda^5} \frac{1}{e^{hc/(\lambda k_B T)} - 1} \tag{1}$$

where h is the Plank constant, c is the speed of light, k_B is the Boltzmann constant, λ is wavelength, and T is the temperature of the body in question. In this case ε represents the emissivity of the body which is a constant and not dependent on wavelength due to the graybody assumption. It should be noted that Plank's Law gives the spectral emissive power normalized on a per unit area, per unit solid angle, per unit wavelength basis. However, since it can be assumed that the filament is emitting an equal amount of radiation per unit of its surface area and per unit solid angle measured with respect to its surface, this is sufficient for estimating the spectrum of radiation that will be seen by the camera.

The total signal that will be seen in a single-color channel is given by Eq.2 as

$$S_1(T) = \int \eta_1(\lambda) B_\lambda(\lambda, T) d\lambda \tag{2}$$

where $\eta_1(\lambda)$ represents the effective camera spectral response for a single color channel, i.e., R, accounting for the lens and filter transmission and $B_\lambda(\lambda, T)$ is the graybody distribution from before. This integration is performed over all wavelengths for which spectral response information

is available or all those over which the camera will capture light, in this case between 375 and 900 nm. Two of these integrated signals can then be taken together to form a ratio given by Eq.3 as

$$CR(T) = \frac{S_1(T)}{S_2(T)} = \frac{\int \eta_1(\lambda)\varepsilon \frac{2hc^2}{\lambda^5} \frac{1}{e^{hc/(\lambda k_B T)} - 1} d\lambda}{\int \eta_2(\lambda)\varepsilon \frac{2hc^2}{\lambda^5} \frac{1}{e^{hc/(\lambda k_B T)} - 1} d\lambda} = \frac{\int \eta_1(\lambda) \frac{1}{\lambda^5} \frac{1}{e^{hc/(\lambda k_B T)} - 1} d\lambda}{\int \eta_2(\lambda) \frac{1}{\lambda^5} \frac{1}{e^{hc/(\lambda k_B T)} - 1} d\lambda} \quad (3)$$

Where the body emissivity ε as well as the Plank constant and speed of light can be pulled out of the integral as constants and canceled out. This equation can then be used to generate a lookup table which relates the color ratio seen by the camera to the temperature of the filament. From the three color channels available only three independent ratios can be created, the exact form of which is completely arbitrary. The three calculated color ratios are shown plotted versus temperature in Figure 5 which also shows the difference between the ratios if no lens or filter were used.

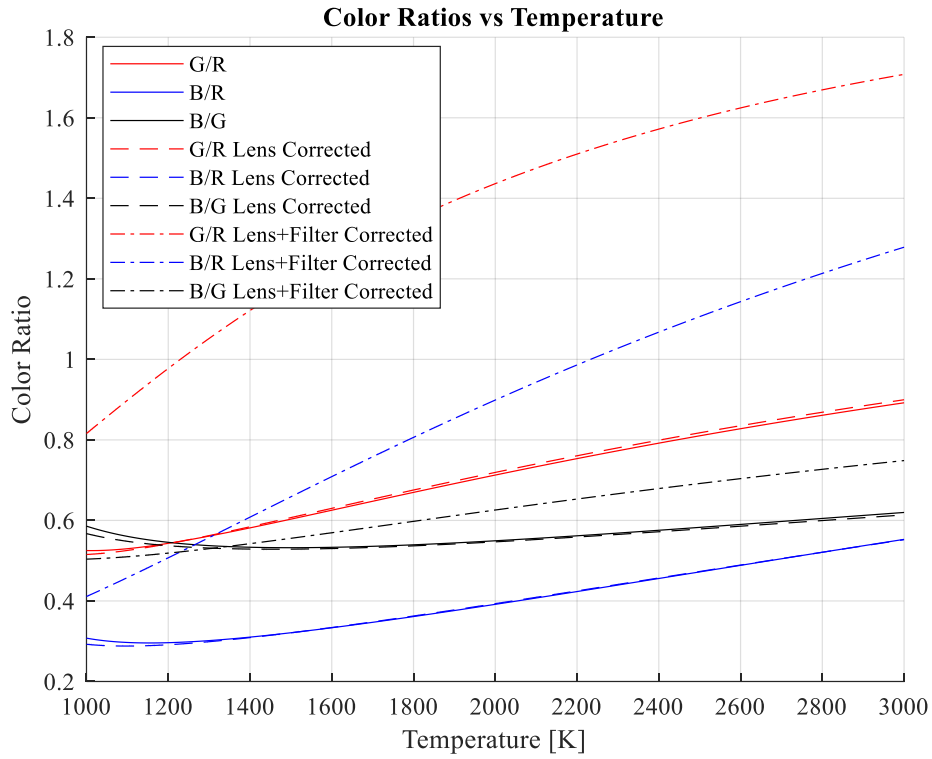

Figure 5: Calculated color channel ratio vs temperature lookup table for Photron FASTCAM NOVA S16 with Nikkor lens and BG-7 filter applied.

As can be seen, there are several issues with the ratios prior to the filter being applied. Specifically, all three ratios are non-monotonic which would lead to significant issues if they were used to interpolate to find temperature. Secondly, the slope of color ratio vs temperature $\frac{\Delta CR}{\Delta T}$ is very low across the full range of temperatures meaning that any noise in the color channel signals will propagate through the interpolation and lead to a very noisy calculated value of temperature. As was intended, the color glass filter fixes both of these issues and, as such, will be used for all results presented in this work.

3.2 Radiation Correction

As mentioned previously, a radiation correction is needed to obtain the actual gas phase temperature from the calculated filament surface temperature. This is a classic heat transfer problem where the fiber is being cooled via radiation loss to the environment and conduction along its length while simultaneously being heated via convection with the surrounding hot gas. The energy balance for this problem is described by Eq.4 as

$$hA_S\left(T_g - T_f\right) = \sigma\varepsilon A_S\left({T_f}^4 - {T_\infty}^4\right) + kA_{CS}\frac{dT}{dr} \tag{4}$$

where h is the convection heat transfer coefficient, σ is Stefan-Boltzmann constant, ε is the total emissivity of the fiber, and k is the thermal conductivity of the fiber. T_g, T_f, and T_∞ represent the gas phase temperature, filament temperature, and ambient temperature respectively while A_S and A_{CS} represent the filament surface and cross sectional areas. Through a basic scalar analysis, it can be shown that conduction along the filament is insignificant compared to the other sources of heat transfer due to the extremely small cross sectional area, low thermal conductivity of the material, and small temperature gradients along the filament. Thus, the temperature of the gas phase may be determined from Eq.5 as

$$T_g = \frac{\sigma\varepsilon\left({T_f}^4 - {T_\infty}^4\right)}{h} + T_f \tag{5}$$

where the conduction term has been neglected. The heat transfer coefficient h can be calculated from the Nusselt number as shown in Eq.6 as

$$h = \frac{Nuk_g}{d_f} \tag{6}$$

where Nu is the Nusselt number, k_g is the thermal conductivity of the hot gas, and d_f is the diameter of the filament. The filament diameter was taken from the manufacturer and the thermal conductivity of the gas was calculated in MATLAB using the open source toolbox Cantera. The mean equivalence ratio at each condition as recorded by LabVIEW was used to determine the appropriate species fractions for the unburnt gas. Temperature and pressure were set to ambient atmospheric values before the gas model was allowed to equilibrate and the needed properties were extracted. Many different Nusselt number correlations can be used but the one chosen for this work is given in Eq.7 from Bergman et al., 2011 as

$$Nu = C{Re_d}^m Pr^{1/3} \tag{7}$$

where $C = 0.989$ and $m = 0.330$ for $0.4 < Re_d < 4$ and $Pr \geq 0.7$.

Chapter 4. Hardware Implementation

4.1 Burner Setup

Testing and verification of the technique was performed using a flat flame burner, formerly known as a McKenna burner, supplied by Holthuis and Associates. This burner is a low flow rate benchtop combustion environment which is designed for use as a calibration standard in combustion studies and is capable of producing a well characterized and repeatable flame. There is also a fair amount of literature data available using the burner which will be used later on as a direct comparison to the results generated through this work. Literature also suggests that these burners usually have mean deviations in the range of 11 to 20 K but in one case an average deviation of 26 K was seen (Weigand et al., n.d.). A cross section of the burner is shown in Figure 6.

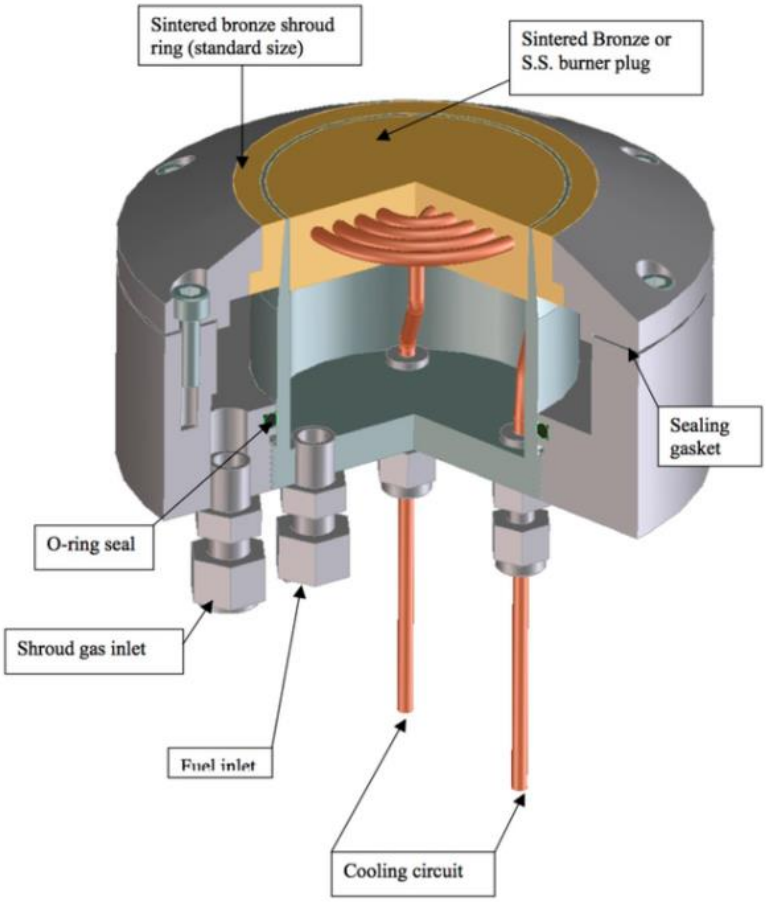

Figure 6: Cross section of the burner showing internal structures and piping.

As can be seen, the fuel and air mixture enters the burner through the fuel port on the bottom before passing through the sintered stainless steel burner plug. This porous medium acts as the anchor point for the flame as well as a flashback suppressor preventing the flame from traveling upstream into the burner or fuel/air supply line. The burner plug is also kept cool by a water loop in the form of an Archimedean spiral which is supplied by an exterior pump and chiller system. The supply inlet and return outlet for the cooling circuit are also located on the bottom of the burner. A second ring of sintered bronze around the outside of the burner plug supplies a flow of shroud gas,

nominally either nitrogen or argon. This flow of inert gas prevents a shear layer from developing around the outside of the flame allowing it to appear truly flat.

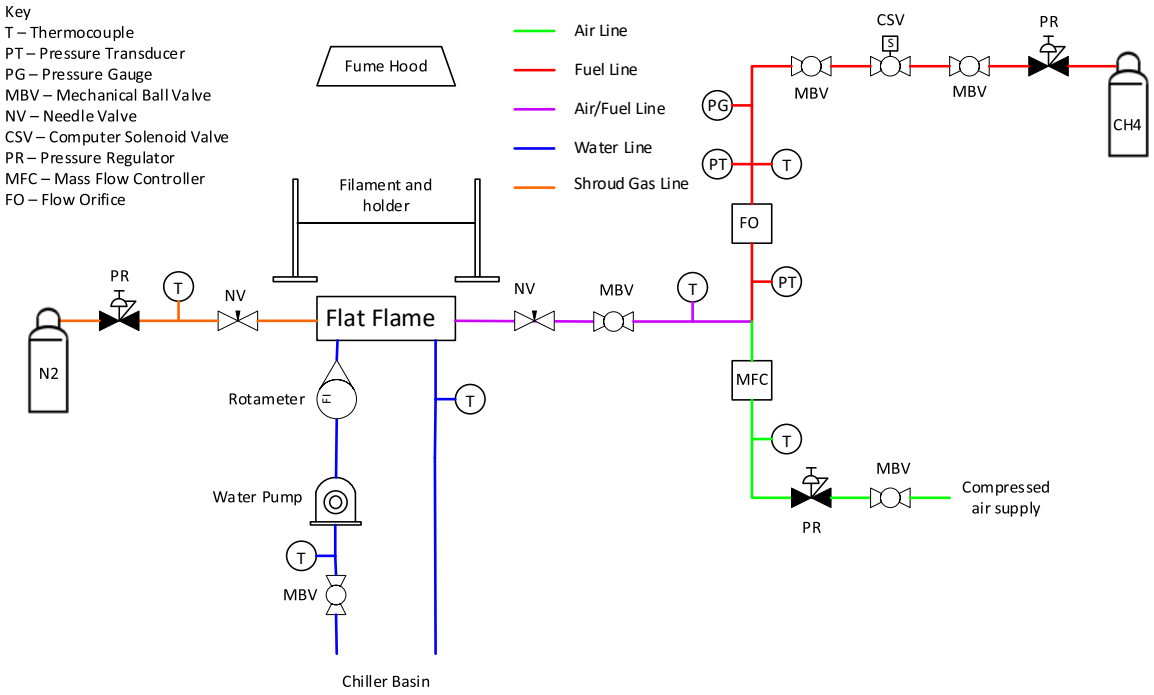

Figure 7: Piping and instrumentation diagram of the burner setup.

A piping and instrumentation diagram (PID) of the burner fuel, air, water, and shroud gas systems is shown in Figure 7. Compressed air is supplied by the facility compressor at around 110 psi. This compressed air then passes through a regulator on the wall of the test cell which can be set from 0 to 150 psi as needed (nominally set at 100 psi). The air is then passed through a mass flow controller (MCR-500SLPM-D-DB15/CM by Alicat Scientific) set to dry air as the operating gas which precisely controls the flow of air in SLPM sent to the burner. A type K thermocouple is also placed just upstream of this mass flow controller (MFC) to alert the operator of any abnormalities such as the regulator freezing or the compressor tank being emptied.

Fuel for the burner, nominally methane, is supplied at pressures up to 2,600 psig by a compressed gas cylinder kept strapped to the wall of the test cell. A pressure regulator fitted directly to the tank reduces the pressure supplied to the fuel line to around 150 psi. Two shutoff valves are installed in the fuel line which can be used to cut the fuel in the event of an emergency. Between these two valves there is also a solenoid operated valve which is controlled via a LabVIEW program and is the direct control used to turn the fuel flow on or off. After the shutoff valves the fuel passes through a precision flow orifice (B-6-BR by O'Keefe Controls) which features a pressure transducer and thermocouple placed just upstream as well as a second transducer just downstream. This flow orifice should always be operated at a choked condition as verified by the pressure transducers meaning that the flow rate of fuel can be determined from Eq.8 as

$$Q_G = Cv\frac{362P_1}{\sqrt{SGT}} \tag{8}$$

where Q_G is the flow rate in standard cubic feet per hour (SCFH), Cv is the flow coefficient of the orifice, SG is the specific gravity of the fuel, and P_1 and T are the upstream pressure and temperature in psia and degrees Rankine. Originally the system was operated using a second MFC to control the flow rate of fuel, however, due to reliability issues and doubts related to its calibration a flow orifice was used instead.

Downstream of the flow orifice, the fuel and air lines are teed together before entering the mixing line leading to the burner. Just upstream of the burner there is a shutoff valve and needle control valve as well as a thermocouple in the air/fuel line. The needle valve is used to restrict the flow into the burner and allow more residence time for the fuel and air to mix properly and provide back pressure to the system. The shutoff valve can be used to immediately extinguish the burner in the event of an emergency while the thermocouple is present to alert the operator of any abnormalities.

Cooling fluid, nominally pure distilled water, is kept in the reservoir of the chiller. The chiller is fitted with an internal pump which is used to prime the loop before the external pump is turned on. A rotameter is fitted vertically downstream of the exterior pump which is used to measure the flow rate of the cooling fluid. Lastly, a type K thermocouple is placed in both the supply and return lines which may be used to monitor the performance of the chiller and burner.

The shroud gas, nominally nitrogen, is supplied at up to 2600 psig by a second compressed gas cylinder kept next to the fuel cylinder on the wall of the test cell. Another regulator fitted to the cylinder reduces the line pressure to around 50 psi. A needle valve just upstream of the burner is used to qualitatively control the flow of shroud gas. Another thermocouple is placed just upstream of this valve again to diagnose any issues with the regulator or gas cylinder.

4.2 Filament Setup

The determination of filament type and manufacturer that would be used in this work was influenced largely by the literature review that was performed in the early stages. In general, monofilaments of silicon carbide have been used historically as opposed to braided or woven filaments due to them having consistent properties along their length and better resistance to degradation over time. While there are many options that would meet these criteria, in this case the SCS-Ultra from Specialty Materials Inc. was selected. These exact filaments have been used in previous applications of thin filaments pyrometry and were shown to have a low sensitivity to aging in the flame as well as a relatively constant emissivity over the wavelengths of relevance (Ma et al., 2013a). The filaments are made from beta silicon carbide deposited onto a carbon monofilament core and have a diameter of 75 μm and a tensile strength of 5,900 MPa. A tensioning stand to keep the filaments taught and stable in the flame while not interfering with the burner was made from 80/20 extrusions and is shown in Figure 8.

Figure 8: Tensioning stand used to keep filaments at the correct height above the burner.

Filaments are passed through holes in the bolts on either upright support and are held tight before being secured with nuts and washers. In the configuration shown, and for all testing performed in this work, the filament is held at 15 mm above and parallel to the top of the burner plug. However, this system could easily be altered or expanded in the future to support multiple filaments at any height that is desired.

4.3 Camera Setup

As mentioned, the camera used as the detector in this application was the FASTCAM NOVA S16 by Photron. This camera features a 1 megapixel CMOS sensor and an ISO of 16,000. It has a dynamic range of 12-bits for each color channel and the images were saved as 16-bit .tiff files to ensure that the full range was captured. All image, sharpening, brightening, or filtering as well as any color enhancement, balance, or correction settings were all turned to neutral or off within the control software prior to taking any data. For the vast majority of testing, images were captured in short bursts of ten seconds yielding 100 images which were then averaged in post processing to reduce the impact of flame flicker or other noise. Exposure time ranged from 0.5 to 2 ms and was set in order to maximize the signal from all three channels while not saturating any of them. The camera was also fitted with an AF Micro-Nikkor 60mm f/2.8D lens set to an aperture of f/5.6. Lastly, the camera was also mounted on a tripod in order to maintain stability and position over the course of testing sessions. The complete setup shown with the burner can be seen in Figure 9.

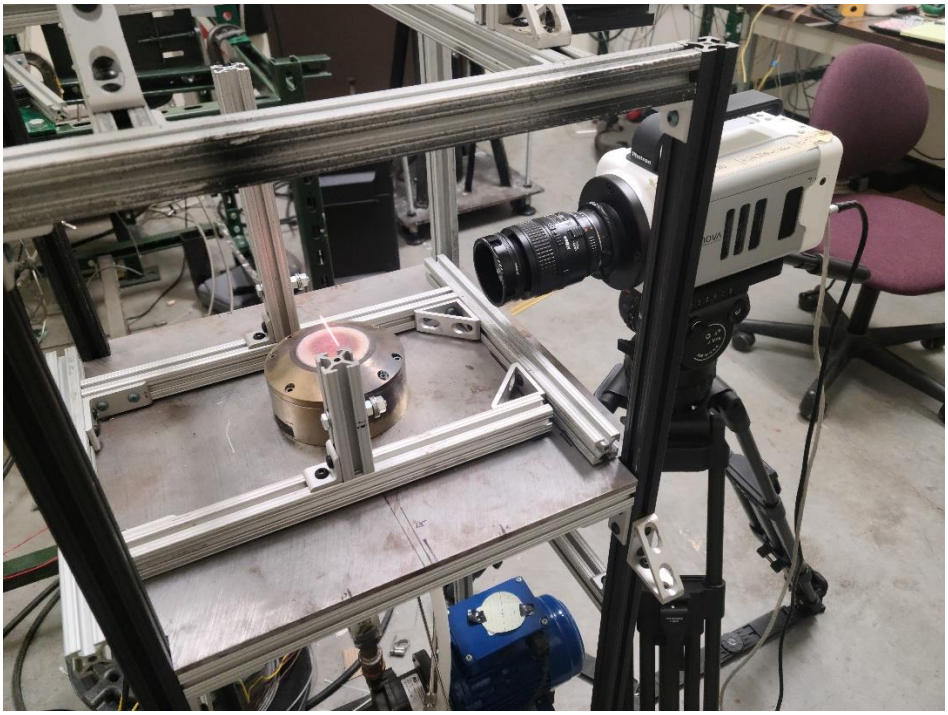

Figure 9: Camera, lens, and filter setup shown with tripod in position to take images.

In order to verify the linearity of the camera response with respect to exposure time, images were taken of a white light source with increasingly longer exposures until all channels were fully saturated. The results can be seen in Figure 10 which clearly shows the expected linear behavior for each channel up until the point of saturation.

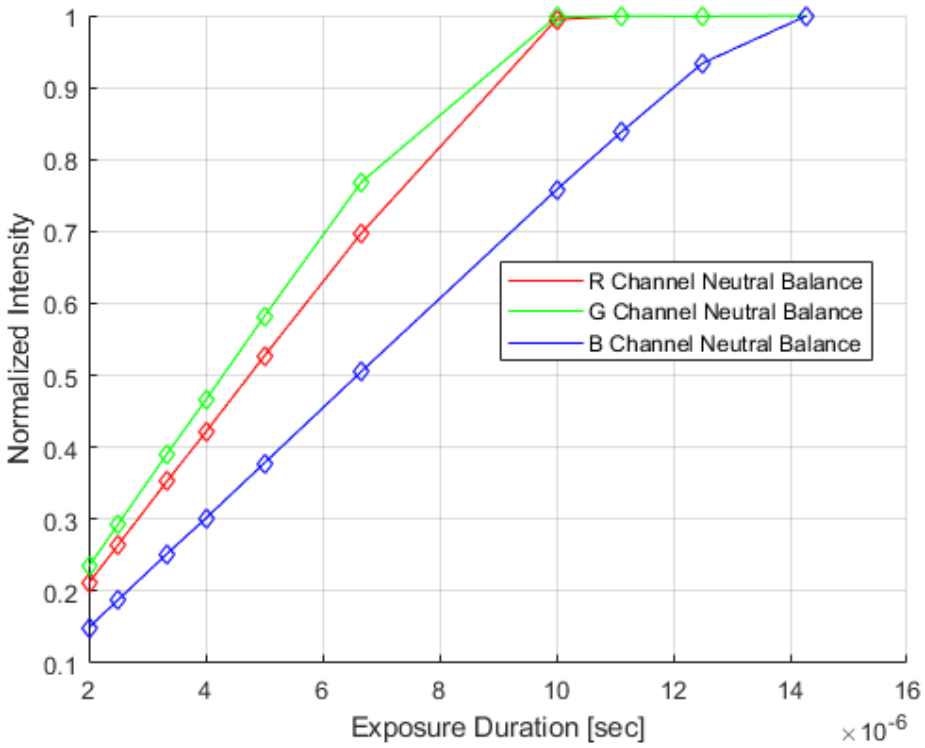

Figure 10: Normalized intensity for each color channel vs exposure time.

When viewed as color ratios as shown in Figure 11 it can be seen that all three ratios are fairly linear with the ratio of green to red being the best of the three.

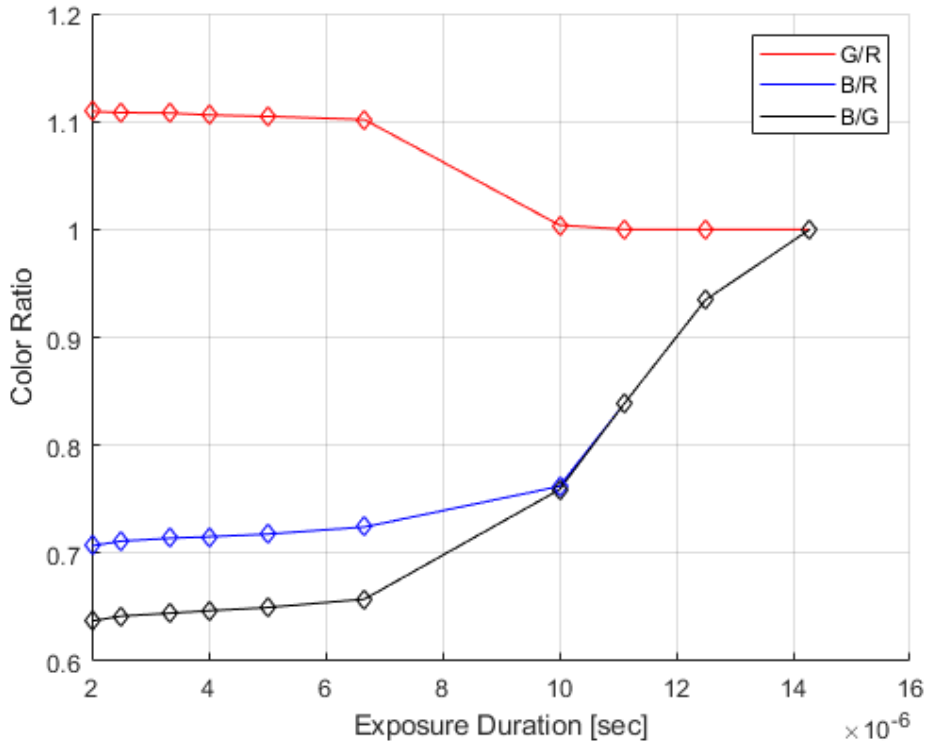

Figure 11: Color ratios versus exposure time.

In addition to verifying the response of the camera with respect to exposure time, it was also essential to verify its spectral response in addition to the transmission curves applied by both the lens and filter. This was done using a light source with a known spectral power distribution. In this case a LEDH-6500 from Lightspeed Technologies was used the power distribution for which is shown in Figure 12.

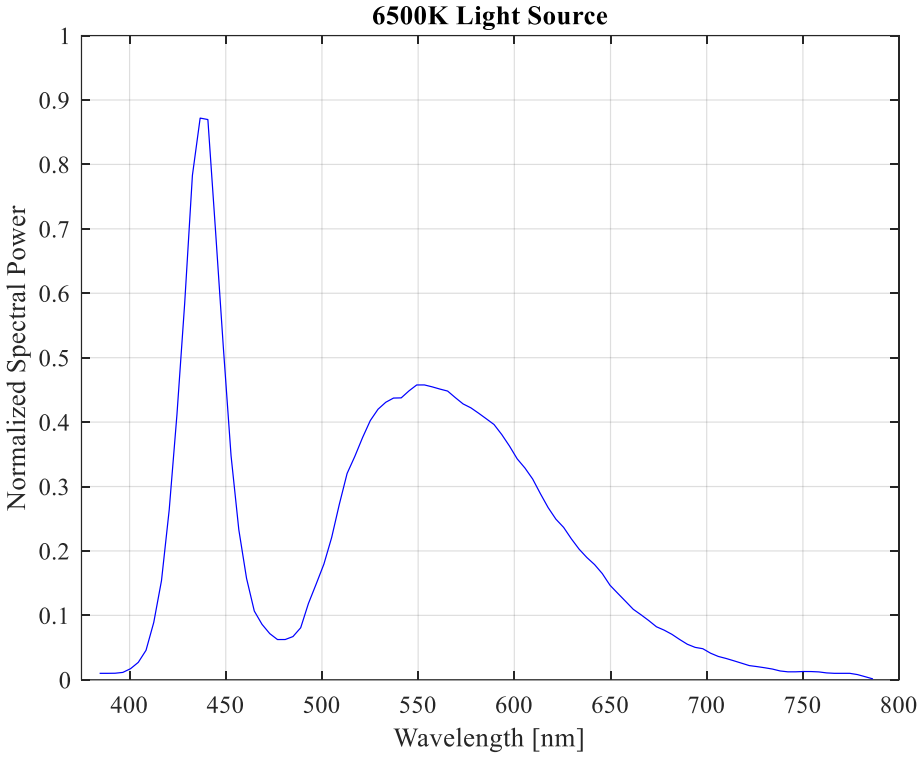

Figure 12: Normalized spectral power distribution for LEDH-6500 light source.

The expected value was calculated using Eq.2 with the light source power distribution in place of the graybody spectrum. Color ratios were taken using the results and these calculated ratios are shown compared to ratios extracted from images taken of the light source in Table 1.

Table 1: Color ratios from signals measured and signals calculated.

	Without Filter		**With Filter**	
Color Ratio	**Calculated**	**Experimental**	**Calculated**	**Experimental**
G/R	1.2617	1.2162	1.9061	1.8550
B/R	0.8909	0.7679	1.6463	1.4202
B/G	0.7061	0.6314	0.8637	0.7656

This data shows that the measured ratios match fairly well with the theoretical calculated results, especially for the G/R ratio. The B/R and B/G ratios however are slightly lower than expected by an average of 10-15%. This suggests that either the spectral response of the camera for the blue channel or either the filter or lens transmission curves are causing the blue signal to be lower than expected. Unfortunately, while this verification process can give some idea of relatively how accurate these response and transmission curves may be, it does not provide a framework for correcting them. In the future a well characterized emission source should be used to verify these curves on a per wavelength basis and the results used in place of the manufacturer provided curves to improve the accuracy of the technique.

Chapter 5. Software Implementation

5.1 Calculation of Temperature Profiles from Raw Images

All post processing for this work was done using MATLAB R2022b along with the appropriate image processing, statistics, and machine learning toolboxes. The set of images from each condition were read one by one before being split into arrays for each color channel and normalized from their 16-bit format to a 0 to 1 double precision format. Each color array was then stored in a three-dimensional array thus saving the data from all images for that condition. The pixel by pixel mean value and sample variance were then calculated which helped to reduce the noise induced by several factors including the flame flickering or flow rate variations. The sample variance will be used later in the Propagation of Errors section to calculate the uncertainty associated with the temperature measurement.

A Gaussian filter was then applied to each mean array for each color channel which had a size of 3x25 pixels with the longer dimension being orientated along the length of the filament. This filter had a standard deviation of 0.25 going across the filament and a standard deviation of 6 along it. This was done in order to reduce any noise factors that would not have been taken care of by the image averaging process such as inconsistencies in the manufacture of the filament along its length leading to higher or lower local intensities. Lastly, thresholding was performed with any values in the mean color channel arrays below a certain limit being set to zero. Through this process any non-zero values in the background due to camera sensor noise or similar factors were eliminated completely. The effects of the image averaging, filtering, and thresholding processes can clearly be seen in Figure 13 comparing a single raw sample to the final result.

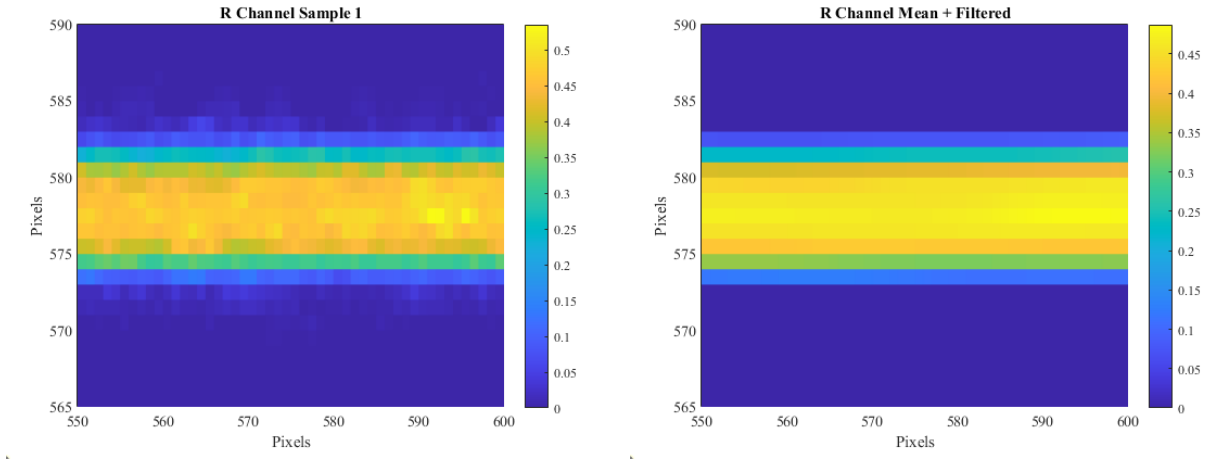

Figure 13: Raw sample versus processed and filtered mean array.

Intensity values for each channel, along the length of the filament, were extracted by taking the maximum value in a vertical band moving from left to right along its length. This was done as it is nearly impossible, especially from a repeatability standpoint, to perfectly align the filament and the detector such that all filament intensity values are captured by a single horizontal band of pixels. In reality, the filament intensity is usually spread over several horizontal bands with the band containing the maximum intensity changing over the width of the image. Previous applications of thin filament pyrometry found in the literature faced a similar issue and used either

the maximum, or the mean, or an integration of channel intensity over a smaller vertical band surrounding the filament. However, in this work the maximum was found to produce the most consistent results and, as such, is what was used for all results presented. Extracted maximum intensity values for each channel are shown for an example condition in Figure 14. This example condition was for a flow rate of 25 SLPM of air and an equivalence ratio of one.

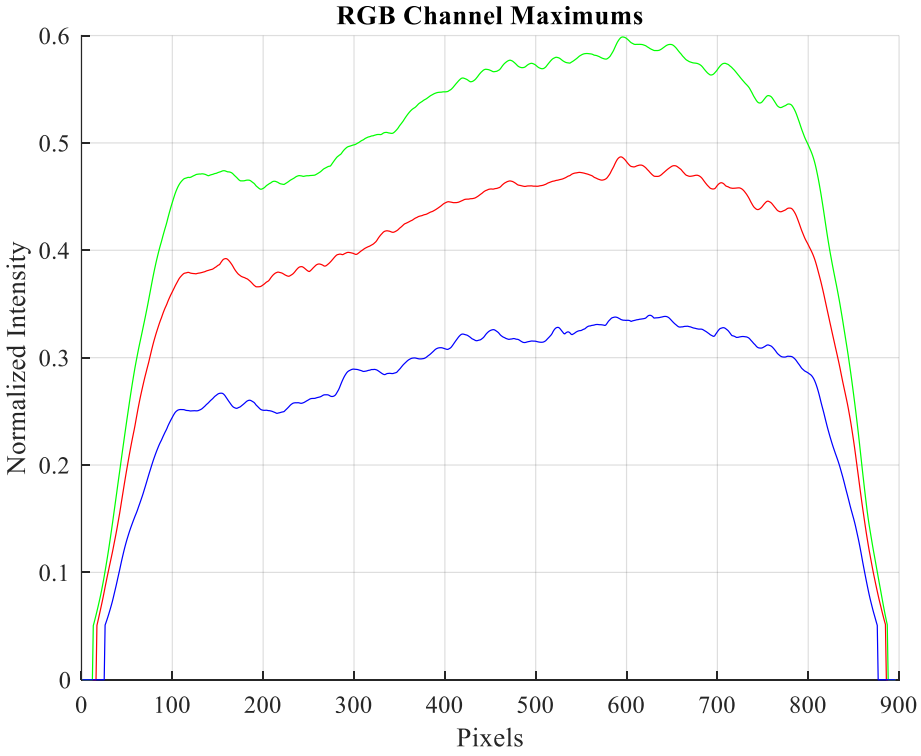

Figure 14: Extracted RGB channel maximum intensity values along the filament for one condition.

The value of sample variance was also extracted for each channel at the same array index where the maximum value was located. This extracted variance along the filament is shown for the same condition in Figure 15. As can be seen, the variance is largest for each channel near the ends of the filament which makes sense since this region will see the greatest effects of flame flicker and any shear layer that develops.

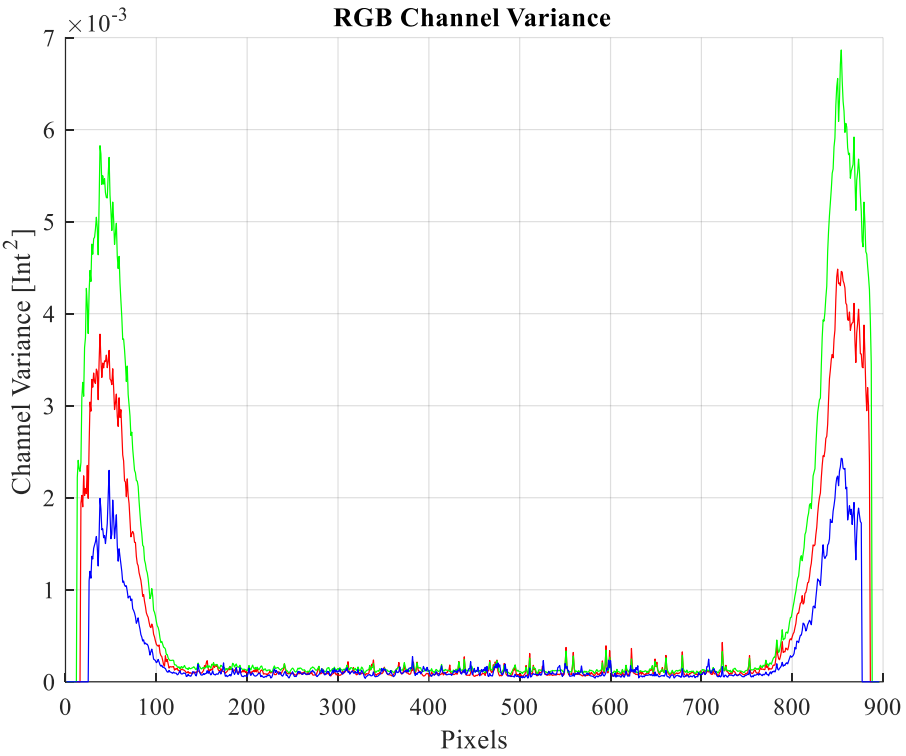

Figure 15: RGB channel variances extracted at the same pixel locations as maximum values.

Color ratio profiles were calculated from the maximum intensity profiles and any undefined values were set to zero. Undefined values were only ever seen near the ends of the filaments where the pixel value from only one channel used in the ratio had been set to zero by the thresholding process. The three-color ratio profiles for the same example condition are shown in Figure 16.

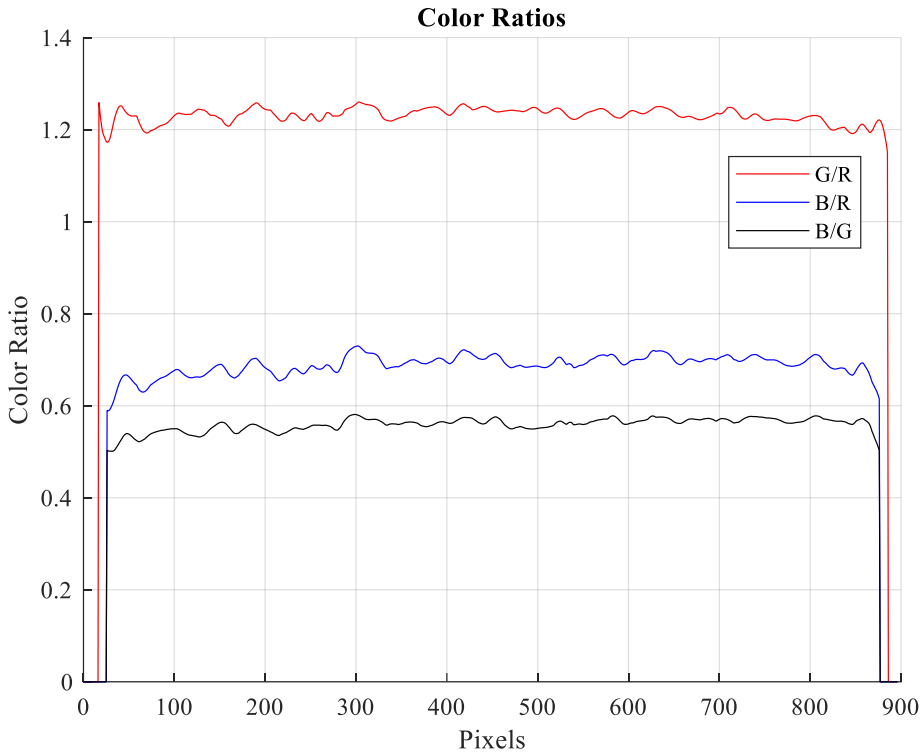

Figure 16: Color ratio profiles calculated from channel maximum intensity profiles.

Uncorrected temperature profiles were generated from the color ratios via a one dimensional linear interpolation using the temperatures and theoretical color ratios calculated from the camera and filter spectral response. Alternative interpolation methods such as cubic or spline were tested but had virtually no effect on the final result due to the small spacing of temperature values (ΔT = 1 K) used in the calculation of the theoretical ratios. The pixel spacing of the profiles was converted to a physical spacing using a calibration image of the burner and filament taken prior to testing. As a result, the physical precision of the current implementation can be stated as 0.06 mm being the spacing between calculated temperature values. Uncorrected temperature profiles generated from the three ratios are shown in Figure 17.

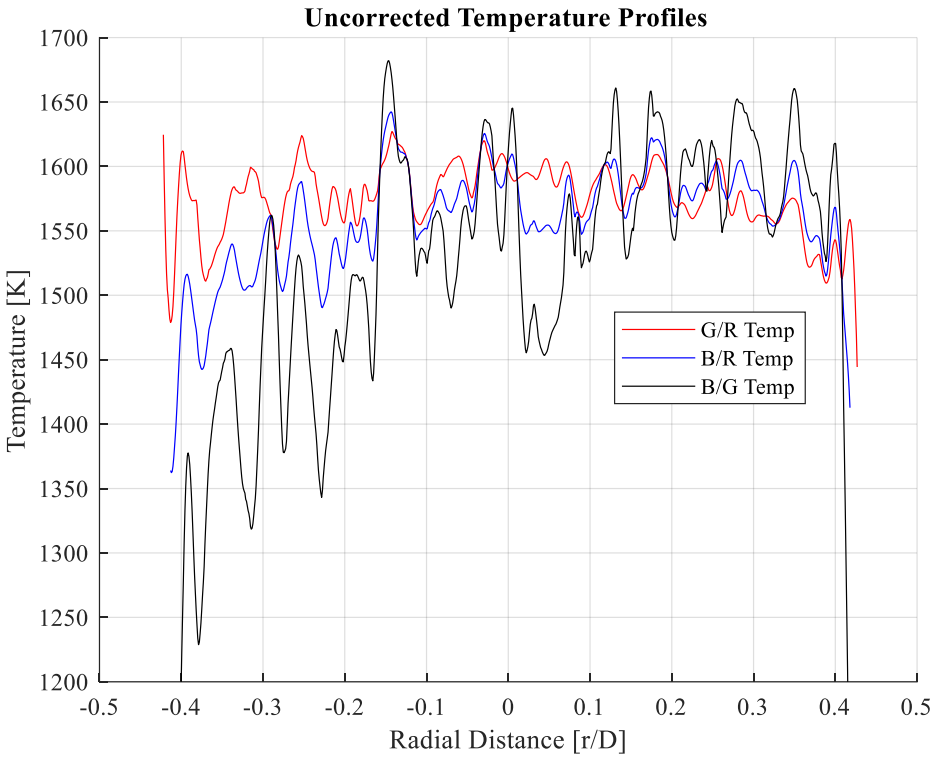

Figure 17: Uncorrected filament temperature profiles generated from color ratio interpolation.

As was outlined in the Background and Methodology chapter, a radiation correction is needed to calculate the actual gas phase temperature from the uncorrected filament temperature. During testing the LabVIEW program was used to record the flow rates of both air and fuel for each condition. The mean flow rate values and the calculated equivalence ratio were used in conjunction with the Cantera toolbox to calculate the density, thermal conductivity, viscosity, etc. of the reacting gas as well as the appropriate Reynolds and Prandtl numbers. The total emissivity of the filament was taken as a literature value for silicon carbide of 0.716 (Balat-Pichelin & Bousquet, 2018). Gas phase temperatures for the same example condition after the radiation correction are shown in Figure 18.

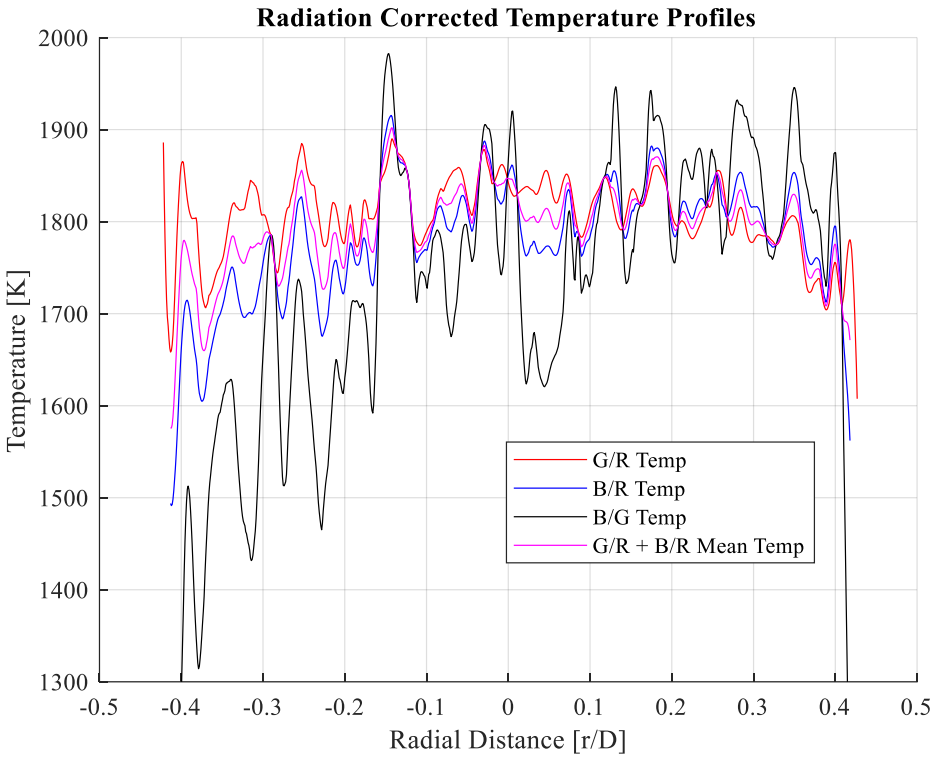

Figure 18: Radiation corrected gas phase temperatures for all three color ratios as well as the mean of the G/R and B/R profiles.

While it has been shown up to this point that all three color ratios can be used to generate reasonable temperature profiles, a decision had to be made as to which should be used as the final result. In different literature sources oftentimes only a single ratio was used or considered while a few sources elected to average all three. In this work the decision was made to use the average of the G/R and B/R temperatures for any results from this point forward. This was based on the fact that these two ratios generated temperatures that were similar not only to each other but to literature data as well as will be discussed later. Additionally, the B/G profile is clearly the noisiest of the three and it would have been undesirable to have this contaminate the final result.

5.2 Propagation of Errors

In addition to verifying the accuracy of the technique through a comparison with literature or other sources of data, it was also equally important to verify its uncertainty through an error propagation study. This was done using the variance or sample variance of each input parameter and analyzing how it would affect the variance of the final temperature result. For this the propagation of variances formula was used as taken from Ku, 1966 and given in Eq.9 as

$$\sigma_f{}^2 = \left(\frac{\partial f}{\partial x}\right)^2 \sigma_x{}^2 + \left(\frac{\partial f}{\partial y}\right)^2 \sigma_y{}^2 + \left(\frac{\partial f}{\partial z}\right)^2 \sigma_z{}^2 + \cdots \tag{9}$$

where the parameters $\sigma_f{}^2$, $\sigma_x{}^2$, $\sigma_y{}^2$, and $\sigma_z{}^2$ represent the variances of f, x, y, and z respectively for $f(x, y, z, \dots)$. This formula allows for the variance of the function f to be calculated as long as

the form of f as well as the variances of its input parameters are known. This also assumes that all input variables are statistically uncorrelated which is a valid assumption in this case.

The first source of uncertainty that was examined was that of the pixel by pixel sample variance calculated from the population of images for each condition. For this methodology to be considered valid, the distribution of sample values around the mean needed to be Gaussian in nature across the entire image as verified by inspection. Histograms of color channel values for a single condition's one hundred image population are shown in Figure 19 both for a point near the center of the filament and near the end where the uncertainty is largest.

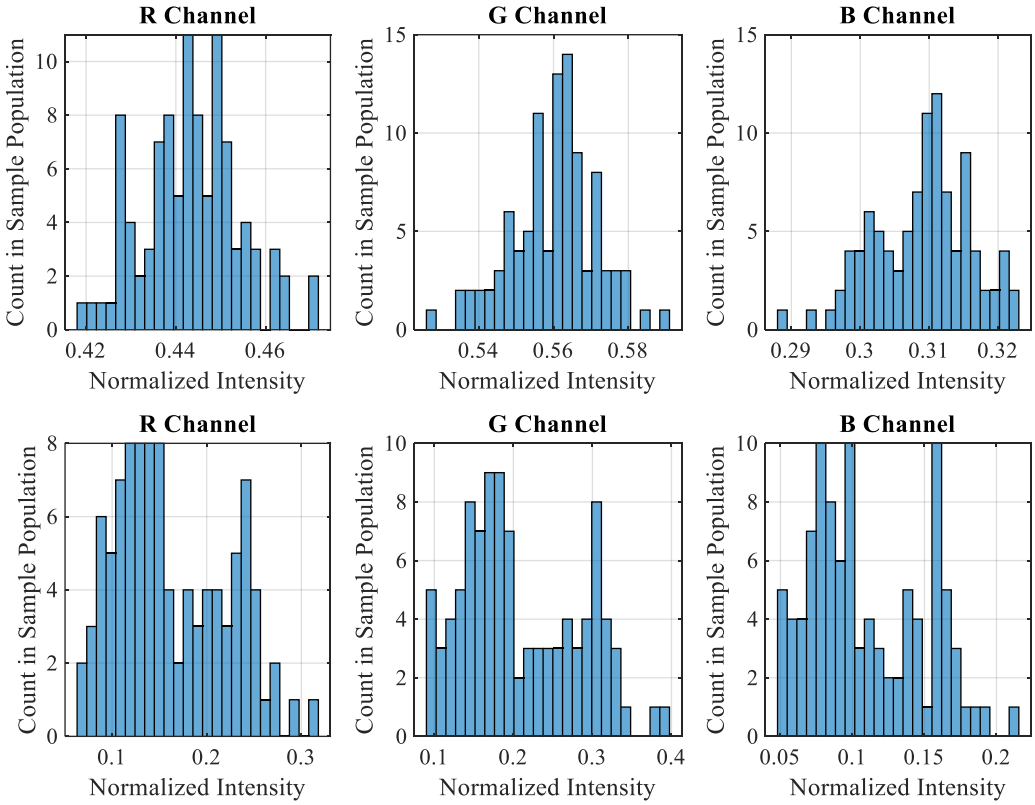

Figure 19: Histograms of channel intensity values for all samples shown for middle (above) and end (below) of filament.

As can be seen, the distributions of channel intensity values for the region near the center of the filament are fairly normal in nature and are close enough to Gaussian to validate this method of error propagation. The distributions of intensity values near the ends of the filament however do not show this behavior. This should not be an issue since the end points are not used in the calculation of any results. Additionally, it may be a good idea in any future work to record more images and once again analyze the distributions of intensity to better support these statements. The process for extracting channel intensity values along the filament in addition to the appropriate variances has already been described in the previous section. The determination of color ratio variance from the individual channel sample variances may be achieved using Eq.9 and the formula for color ratios given in Eq.10 as

$$CR_{G/R} = \frac{G}{R} \tag{10}$$

Where $CR_{G/R}$ is the color ratio, in this case that of green to red, and G and R represent the maximum values extracted along the filament. In this case the derivative terms are trivial to calculate and are given by Eq.11 and Eq.12 as

$$\frac{\partial CR}{\partial G} = \frac{1}{R} \tag{11}$$

$$\frac{\partial CR}{\partial R} = -\frac{G}{R^2} \tag{12}$$

leading to the definition of color ratio variance given in Eq.13 as

$$\sigma_{CR}{}^2 = \frac{R^2 \hat{\sigma}_G{}^2 + G^2 \hat{\sigma}_R{}^2}{R^4} \tag{13}$$

where $\hat{\sigma}_G{}^2$ and $\hat{\sigma}_R{}^2$ represent the sample variances extracted from the green and red channels respectively. A near identical formula was calculated for the two other color ratios. The color channel variances for the same sample condition are shown in Figure 20.

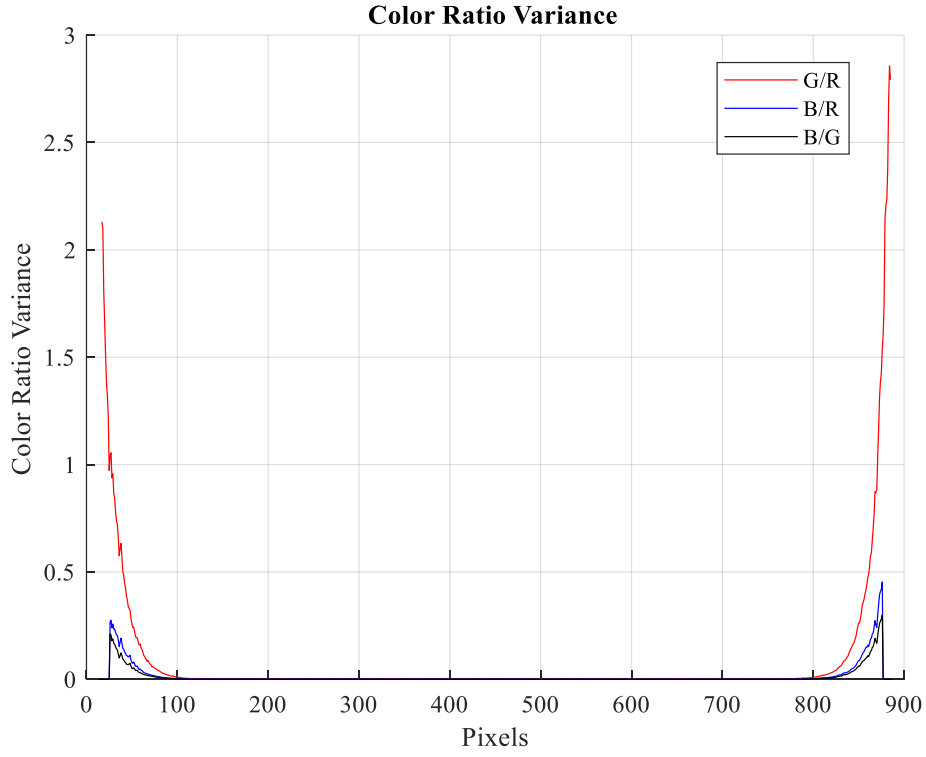

Figure 20: Color ratio variances along the filament calculated from channel sample variances.

Next the color ratio variance needs to be passed through the interpolation process used to determine the filament temperature. Since a linear interpolation method was used, the formula is quite simple and is given in Eq.14 as

$$T_f = \frac{\Delta T}{\Delta CR} CR + T_0 \tag{14}$$

where T_f again is the filament temperature, $\frac{\Delta T}{\Delta CR}$ is the local slope calculated by the interpolation algorithm, and T_0 is the lower of the two points that bound the query point CR. Assuming there is no uncertainty associated with either the local slope or lower bounding point the variance of interpolated filament temperature is given by Eq.15 as

$$\sigma_{T_f}{}^2 = \left(\frac{\Delta T}{\Delta CR}\right)^2 \sigma_{CR}{}^2 \tag{15}$$

where $\sigma_{CR}{}^2$ is the color ratio variance calculated above. This equation was evaluated using the slopes extracted from the interpolation function for each query point for each color ratio profile respectively. The calculated filament temperature variance then needs to be passed through the radiation correction as given by Eq.5. Assuming the only sources of uncertainty are the interpolated filament temperature and the heat transfer coefficient, the variance of the corrected gas phase temperature may be given by Eq.16 as

$$\sigma_{T_g}{}^2 = \left[\frac{4\varepsilon\sigma T_f{}^3}{h} + 1\right]^2 \sigma_{T_f}{}^2 + \left[-\frac{\varepsilon\sigma\left(T_f{}^4 - T_\infty{}^4\right)}{h^2}\right]^2 \sigma_h{}^2 \tag{16}$$

where for clarity ε, σ, and h represent the total emissivity of the fiber, the Stefan-Boltzmann constant, and the heat transfer coefficient respectively. The uncertainty associated with the heat transfer coefficient may be determined from the definition with respect to Nusselt number as given in Eq.6. Assuming that the thermal conductivity of the gas as calculated from Cantera has no associated error, the variance of the heat transfer coefficient may be given by Eq. 17 as

$$\sigma_h{}^2 = \left(\frac{k}{d_f}\right)^2 \sigma_{Nu}{}^2 + \left(-\frac{Nuk}{d_f{}^2}\right)^2 \sigma_{d_f}{}^2 \tag{17}$$

Where k and d_f represent the gas thermal conductivity and the diameter of the filament. A static uncertainty value of 20% was assumed for $\sigma_{Nu}{}^2$ as was suggested by the source for the Nusselt number correlation (Bergman et al., 2011). This may still be conservative, however, given that these correlations are often based on data from a large range of geometries and conditions and are not tailored for one application or another. For the filament diameter a value of 10% was used as was suggested by the manufacturer provided tolerance.

Using the final propagated values of gas phase temperature variance, 95% confidence intervals may be calculated assuming a normal distribution for each color ratio temperature profile. These confidence intervals are shown in Figure 21 for the same example condition used in this chapter.

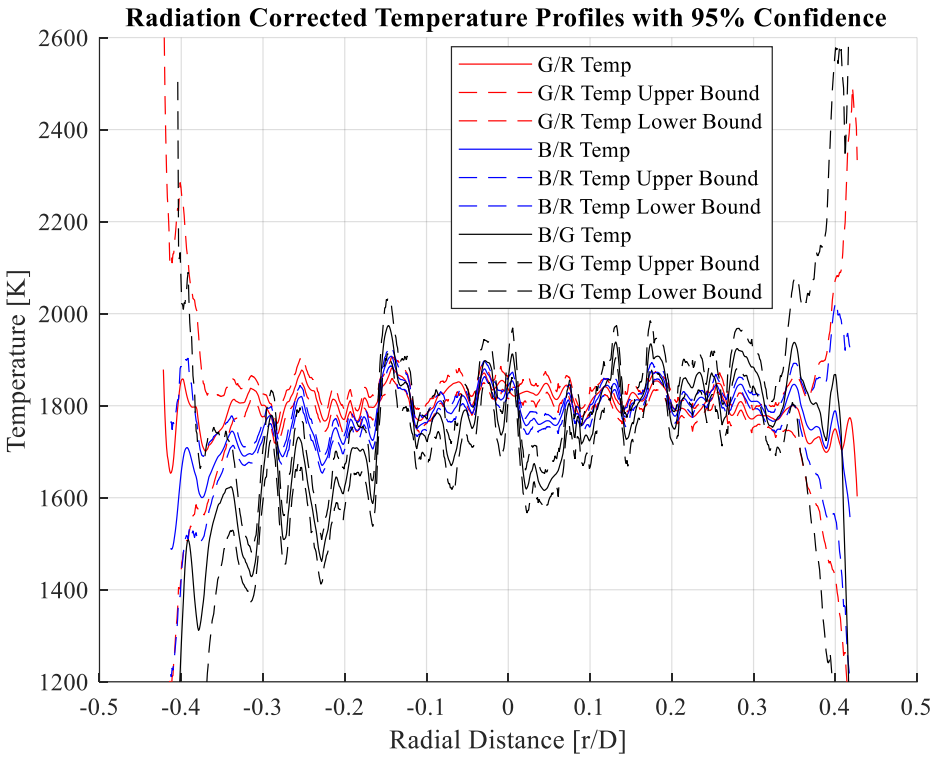

Figure 21: 95% confidence intervals for each temperature profile.

Across the central region of the filament the average uncertainties associated with the G/R and B/R temperature profiles are around ±25 K and ±15 K respectively while for the B/G ratio the average uncertainty is around ±50 K. These uncertainty values are in the same range as those quoted in the literature being ±60K by Maun et al., 2007 and ±45 K by Ma et al., 2013. Fundamentally this would be the error associated with a single pixel or single radial location temperature measurement based solely on the errors introduced by the camera itself and all post processing procedures.

It is also important to understand which of the error sources discussed has the greatest impact in terms of increasing the final error value. As a visual example of this, the confidence interval ranges based on either the filament or gas phase temperature variances are shown in Figure 22. It can clearly be seen that the contribution of the filament temperature uncertainty to the gas phase temperature uncertainty is relatively small. Thus, it can be said that the primary source of gas phase temperature uncertainty stems from the radiation correction and related errors. In future work it would be a good idea to attempt to reduce these errors through the use of a more accurate or condition optimized Nusselt number correlation.

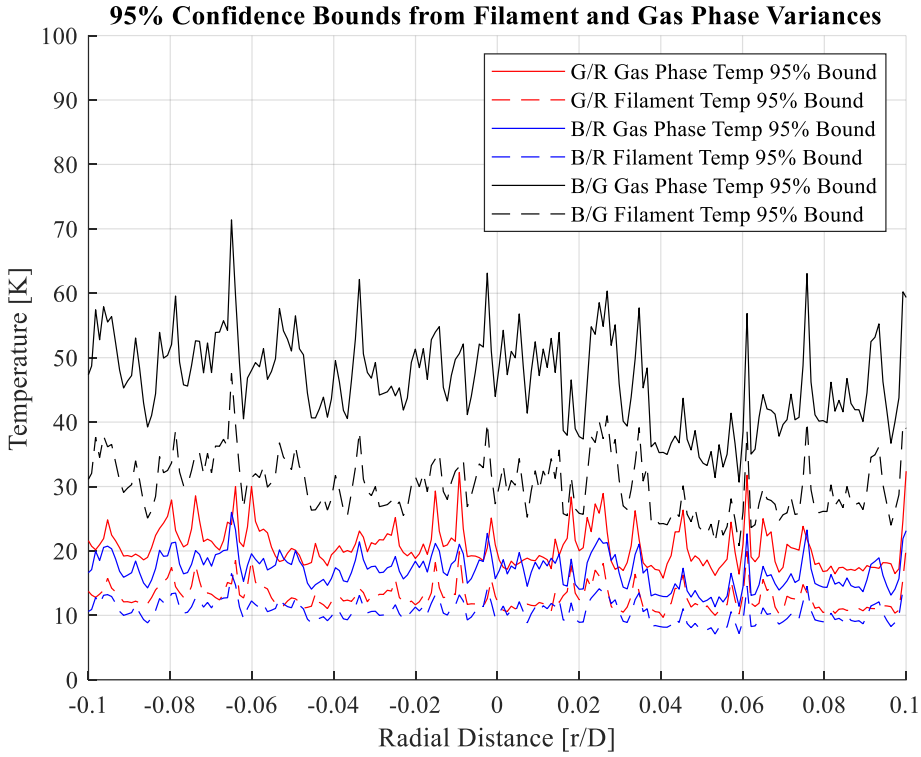

Figure 22: Comparison of 95% confidence bounds for both filament and gas phase temperature variance.

In addition to propagating any sources of error through to the final value of temperature it was also important to look into the sources of error that could affect the flow rates measurements and, as a result, equivalence ratio. For any fuel equivalence ratio may be calculated as defined in Eq.18 as

$$\Phi = \frac{(A/F)_{stoich}}{(\dot{m}_a/\dot{m}_f)} \tag{18}$$

where $(A/F)_{stoich}$ represents the air to fuel mass ratio for stoichiometrically perfect combustion while $\dot{m}_a$ and $\dot{m}_f$ represent the actual mass flow rates of air and fuel. Again, using the method of variance propagation, the variance in equivalence ratio may be calculated as defined in Eq.19 as

$$\sigma_\Phi{}^2 = \left(-\frac{(A/F)_{stoich}\dot{m}_f}{\dot{m}_a{}^2}\right)^2 \sigma_{\dot{m}_a}{}^2 + \left(\frac{(A/F)_{stoich}}{\dot{m}_a}\right)^2 \sigma_{\dot{m}_f}{}^2 \tag{19}$$

where $\sigma_{\dot{m}_a}{}^2$ and $\sigma_{\dot{m}_f}{}^2$ represent the variance associated with the measurement of air and fuel respectively. The appropriate value for $\sigma_{\dot{m}_a}{}^2$ may be determined from the measurement tolerance associated with the mass flow controller. In this case the manufacturer recommends 0.60% of the full range which equates to ±3 SLPM. The determination of $\sigma_{\dot{m}_f}{}^2$ is a bit more complex however and Eq.8 must be employed. Assuming the only sources of error are the measurement of fuel temperature and pressure the variance of fuel flow rate may be determined from Eq.20 as

$$\sigma_{\dot{m}_f}{}^2 = \left(\frac{444}{84946}\frac{816Cv}{\sqrt{SGT}}\right)^2 \sigma_{P_1}{}^2 + \left(-\frac{444}{2(84946)}\frac{816P_1Cv}{\sqrt{SGT^3}}\right)^2 \sigma_T{}^2 \quad (20)$$

where $\sigma_{P_1}{}^2$ and $\sigma_T{}^2$ represent the variance associated with the measurement of fuel pressure and temperature. For this application the formula for mass flow rate from Eq.8 has also been reformulated to return values in g/s as opposed to SCFH. As mentioned, a pressure transducer was used to determine the upstream pressure, in this case a SPT25-10-1000A by Prosense. These transducers are quoted by the manufacturer as having an uncertainty of ± 0.50% of their full range which corresponds to ± 5 psi. A type K thermocouple was used to measure the fuel temperature which is quoted as having an uncertainty of ± 2.2 K.

This set of equations as well as the mean values of temperature, pressure, and mass flow rate for each condition were used to calculate 95% confidence intervals for equivalence ratio and were included in any applicable results along with those calculated for temperature.

Chapter 6. Results and Discussion

6.1 Aging Results

An important property that must be examined for a successful implementation of the thin filament pyrometry technique is that of filament aging behavior. This factor was investigated by many of the literature sources examined in this work and was found in several cases to have a significant effect on the final temperature results. There are two primary factors that both contribute to changes with aging in the flame: coatings applied in the manufacture of the filaments being burned off and the gradual deposition of soot on the filament surface. Coatings of various materials are often applied in order to protect the filaments and to aid in their normal intended use in the garment industry. Soot deposition should be minor within the low flow rate premixed flat flame, however, over a long period of time it can still have a significant effect. Both of these factors can have a large influence on the total surface emissivity of the filament and could even invalidate the graybody assumption leading to different temperature values being seen over time. Examining the aging tests performed on multiple different types of filaments by Ma et al., 2013, it can also be seen that this behavior is not consistent or defined and must be characterized for each filament independently. In order to characterize the filaments used in this work, three aging tests of 30, 30, and 90 minutes each were performed using new sections of filament every run. Nitrile gloves were worn, and care was taken to not contaminate the surface of the filament whenever a new section was installed to the tensioning stand. Data was recorded at regular intervals and the results can be seen for all three tests in Figure 23.

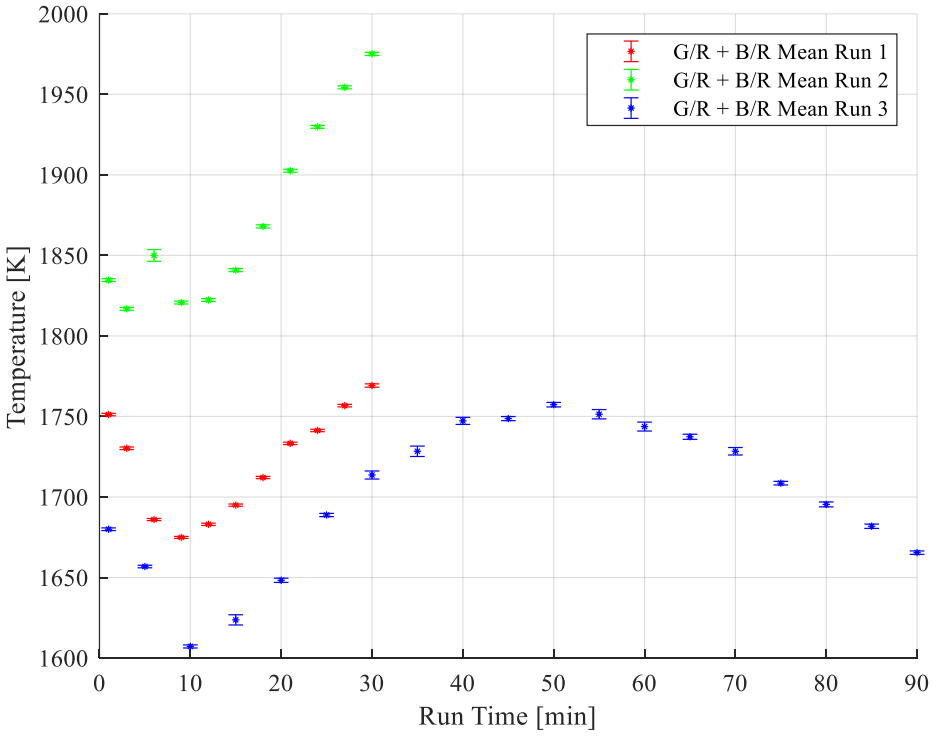

Figure 23: Aging test results for all three runs showing the G/R and B/R mean temperature.

In order to calculate a single temperature result for each condition the G/R and B/R temperature profiles were averaged and then the mean was taken in a 100 pixel band in the center of the filament. A similar behavior can be seen in all three runs – there is an initial decrease in the temperature and then a slower increase before another slow decrease as seen in the 90 minute run. Data from an aging test performed by Ma et al., 2013 is shown in Figure 24 as a reference where a similar trend of a rapid initial change and then a slow gradual shift can be seen.

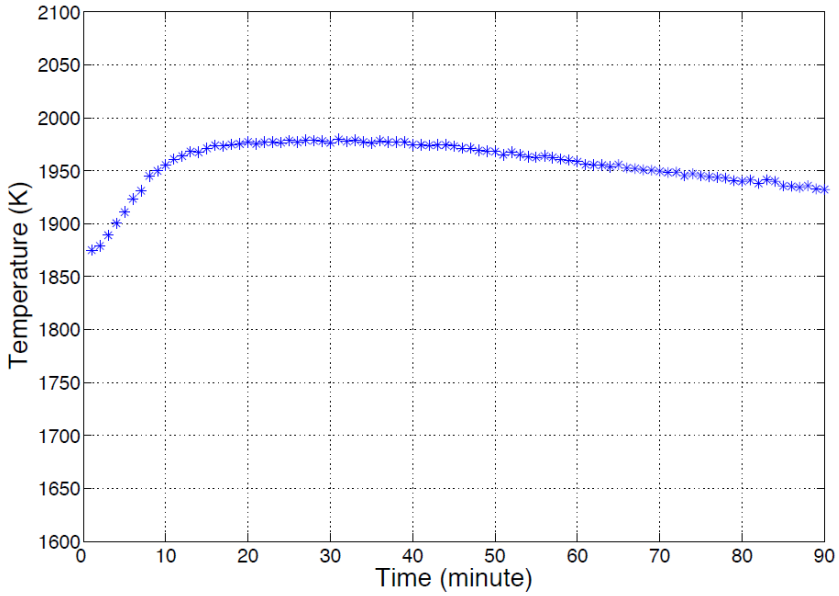

Figure 24: Aging effect of CG Nicalon™ fiber on measured temperature using color ratio TFP (Ma et al., 2013b).

Differences between temperature increases or decreases seen across the same time periods could be due to several factors including the fibers used or the color ratios used to calculate the final temperature. It is believed by the author of this work that the initial period of rapid change is due to the coating being burned off while the period of longer slower change is likely due to soot deposition. However, more testing would be needed to verify this theory. For instance, filaments could be analyzed before and after the first 10 minute period under an electron microscope as was done by Maun et al., 2007 to determine if the coating had been burned off completely. Soot deposition could also be seen on the surface of the filament through this analysis although a longer test may be required before it is visible.

Another factor that is also apparent in Figure 23 is that, while the trends are very similar, the actual values of temperature are shifted by up to 200 K from one run to another. This is contradictory to the results presented in the Propagation of Errors section where the temperature results had a maximum associated uncertainty of about ±50 K. It is believed that, since each run was performed on a different day with the setup being broken down in between, this large shift is due to errors introduced by setup changes. This prevailing issue will be discussed in further detail in the upcoming section.

6.2 Equivalence Ratio Sweep Results

The primary source of literature data that was used for comparison to this work was a study performed by Weigand et al., 2003 which was supported by the Deutsches Zentrum für Luft- und Raumfahrt (DLR). This study used a flat flame burner as in this work and characterized the flame temperature and species concentrations for 22 different conditions through the use of the CARS method. This study provides a good framework for how the flame temperature at a location 15 mm above the burner plug is affected by both equivalence ratio and the total flow rate. The test matrix was generated by cycling through constant fuel flow rates and modifying the flow rate of air to sweep through equivalence ratios. The data presented in the study is shown in Figure 25 where the flow rate of fuel is noted in the legend.

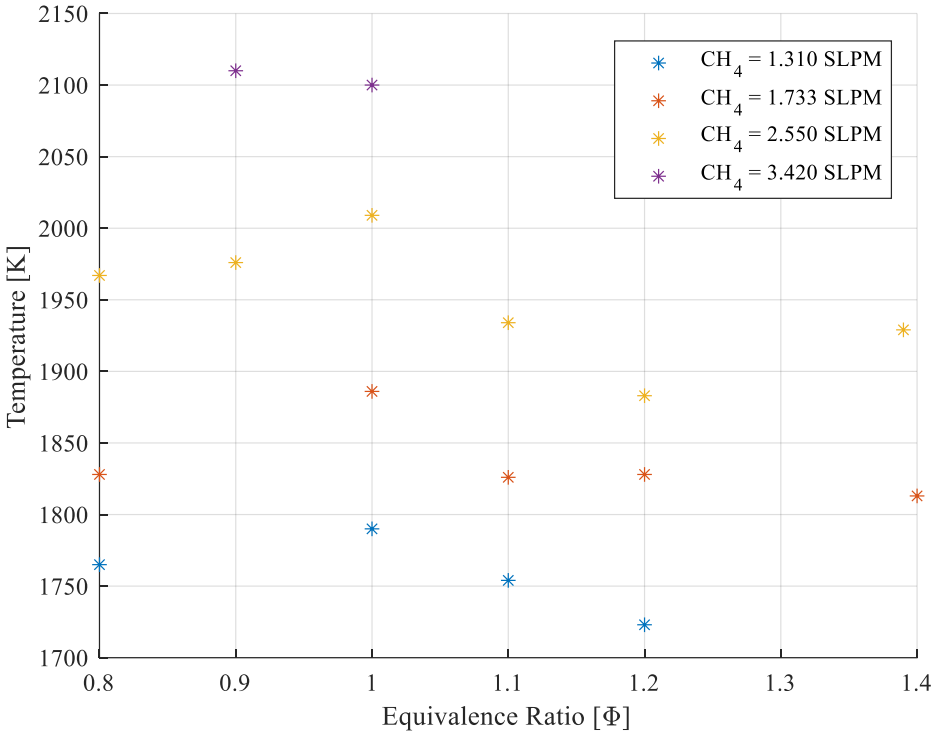

Figure 25: Equivalence ratio versus CARS temperature measurements for different flow rates of fuel (Weigand et al., n.d.).

As can be seen, while the trend remains the same with increasing flow rate the measured temperature increases by as much as 300 K over the full range of conditions. This factor will be considered and discussed whenever comparisons between this data and the results of this work are directly compared.

In a similar fashion to the aging tests, seven equivalence ratio sweeps were performed over three separate days of testing. The sweeps were all performed with filaments that had been aged for a minimum of 30 minutes meaning the behavior should be that of the region characterized by gradual change as seen in Figure 23. The total mass flow rate at each condition where images were recorded was logged in LabVIEW and is shown compared to the most similar DLR data in Figure 26.

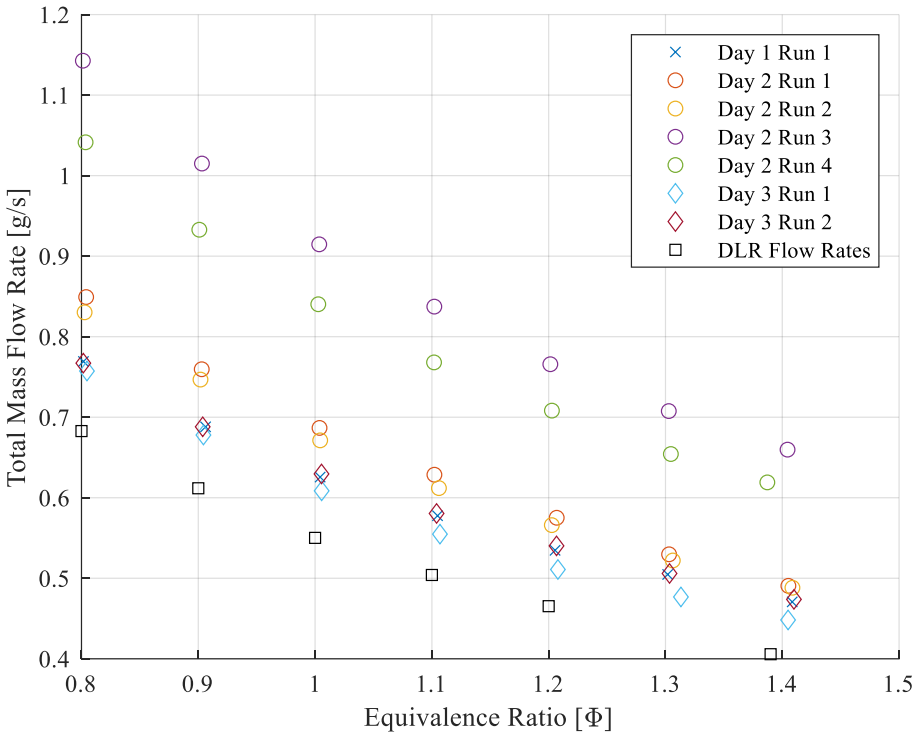

Figure 26: Total mass flow rate vs equivalence ratio for each sweep compared to DLR data.

As can be seen, the total flow rate varied quite a bit from run to run as well as day to day due to the low precision of the fuel delivery system. This was due to issues with the fuel pressure regulator, more specifically the drift in the supply pressure that was seen over the course of the day and especially whenever flow was stopped. To compensate for this and to ensure consistent fuel/air ratios, the air MFC was configured to adjust its flow rate based on the measured flow rate of fuel to maintain an equivalence ratio set in the code.

The G/R and B/R mean temperatures were extracted along a 100 pixel band in the center of the filament and the average was taken as was done for the aging test results. These results are plotted for each run compared to the DLR CARS measurements in Figure 27.

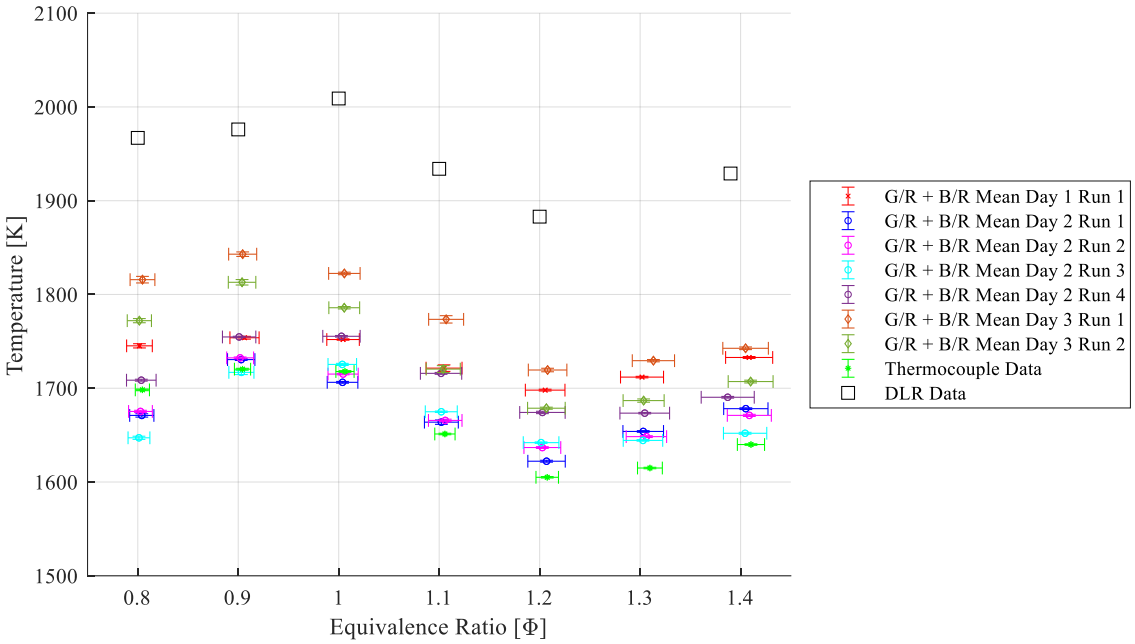

Figure 27: G/R and B/R mean temperatures versus equivalence ratio for all equivalence ratio sweeps.

In addition to the thin filament pyrometry measurements, data taken from equivalence ratio sweeps performed on the burner with a type B thermocouple is shown for comparison. Temperature values recorded by the thermocouple were averaged over a two-minute period at each condition and corrected for radiation in the same manner as the filaments. Three sweeps were performed with the thermocouple which were averaged together, and 95% confidence bounds for both temperature and equivalence ratio were calculated also in the same fashion as for the filament measurements.

While the divergence from the DLR measurements of the TFP data is supported at least to some extent by the thermocouple data, what is not evident is the cause of the deviation seen day to day or run to run uncontrollable variables in the system setup and variations in total flow rate due to the method of maintaining equivalence ratio constant. While the total difference in the temperature values from one day to another sees a maximum value of around 100 K, error propagation analysis would suggest these differences should be within ±5 K with the current population of sample points. This leads to the conclusion that, while error propagation is sufficient for describing the uncertainty introduced by the post processing steps, it is incapable of describing the deviations seen in the technique through actual implementation.

In order to visualize the actual uncertainty associated with the technique on an implementation basis, the G/R and B/R mean temperatures for all seven runs were averaged and the sample variance was calculated. The same was done for equivalence ratio and a Student's t-distribution was used to calculate 95% confidence bounds based on the sample variances. The results are shown in Figure 28 again compared with the thermocouple and DLR data.

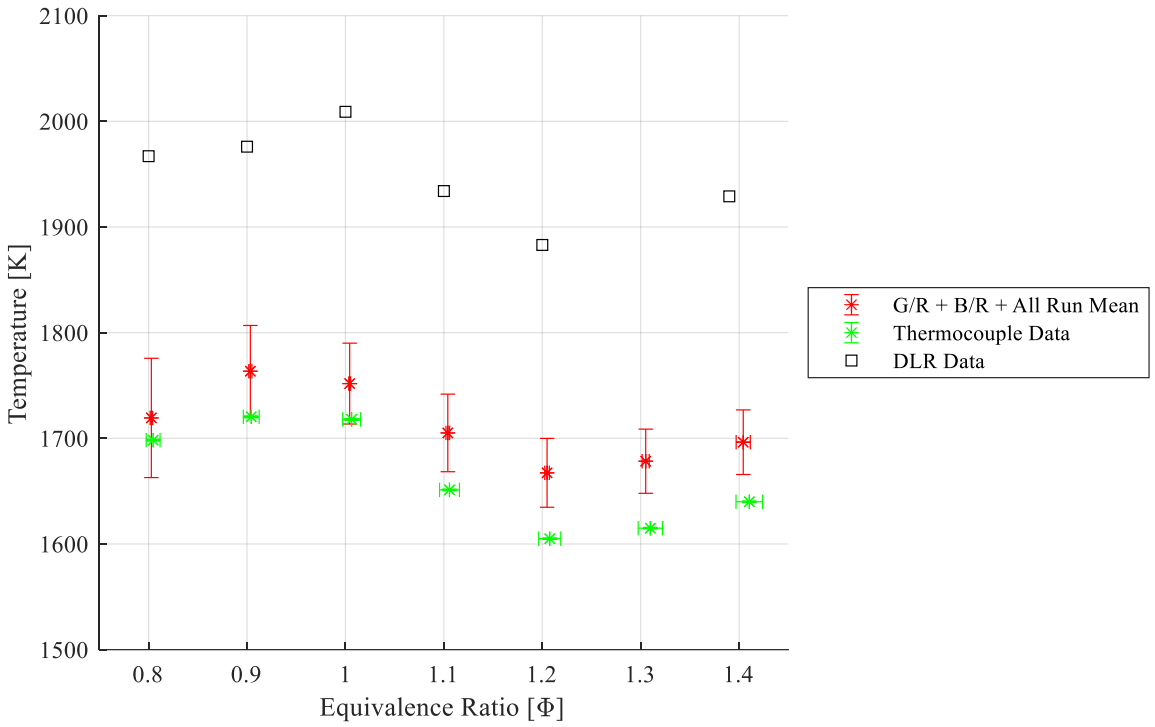

Figure 28: Average temperatures from all runs and 95% confidence bounds from Student's t-distribution.

As can be seen, the uncertainty associated with equivalence ratio is fairly low but there is an uncertainty of about ±55 K associated with the mean temperature values. This represents the approximate bounds within which any future data should fall when accounting for the day to day errors induced by inconsistencies in either the setup or the environmental conditions. While this is still not a very high degree of accuracy, it may be acceptable for a variety of applications, especially considering the simplicity of the technique. Additionally, many suggestions for improving the day to day accuracy as well as resolving the disagreement with DLR data will be proposed and discussed in the last chapter.

Chapter 7. Conclusions and Future Work

The work done in this thesis details the progress made towards the implementation of the thin filament pyrometry technique using a commercially available CMOS camera and other readily available non-custom components. The technique was developed through an analysis and amalgamation of past methodologies detailed in the literature with the addition of some new methods and processes. Verification of the technique was done through the use of well characterized calibration flame and the results were compared to literature values measured on a very similar setup. While the temperature results diverged somewhat from the literature values, they were verified through the use of a thermocouple on the same setup as the pyrometry measurements. A detailed statistical analysis of the various sources of error yielded large but fair confidence intervals for the results which were within reason considering the uncertainty values cited in the literature for previous applications of the technique. These uncertainties are also fairly reasonable when compared to the expected error of other techniques that could be used to deliver similar measurements of flame temperature. While there are certainly still many improvements that could be made, the analysis presented in this work would suggest that this implementation is at a point where it can be applied in other laboratory experiments for estimating temperature profiles of flames.

An outline of the future work needed to improve the technique could be divided into three major categories: improvements to the optics setup, additions or changes to the burner setup, and advancements that could be made to verify and improve the technique itself.

Possibly the largest assumption that is essential to the current formulation of the technique is that the spectral radiance produced by the filament at a given temperature is that of a graybody. To reduce the influence of this assumption, bandpass filters could be used to reduce the band of wavelengths that are captured by the camera. While it may be a stretch to assume that the filaments have a constant emissivity over the current full range, reducing this range even by half would make such an assumption far more reasonable. To build on this, an image doubler could be used to split the signal from the filament into two identical images, each of which would be passed through a bandpass filter before being synchronously recorded by the camera. In this case the ratio of the integrated bands and color channels they encompass could be used to form a ratio and then interpolated to determine temperature. This would allow the bands to be even narrower thus reducing the dependence on the graybody assumption even further. Lastly, the use of a calibrated blackbody emitter to verify the camera and filter response curves would be essential to improving the confidence in this technique.

With regards to the burner setup and the fuel and air systems that supply it, several improvements could be made to increase both accuracy and repeatability. The mass flow controller should be calibrated in order to ensure that it is delivering the stated flow rate. Additionally, a smaller or more appropriately sized MFC could be used as the associated measurement error is a percentage of their full range. For the same reason a more appropriately sized fuel pressure transducer should be used to reduce the uncertainty associated with the fuel flow rate.

It is the opinion of the author that the largest lingering question from this work is the source of the differences seen in results day to day as well as compared to DLR data. To answer half of this a

third technique, CARS or chemiluminescence for example, could be used to measure the temperature of the flames produced by the burner and compared to current results. With some of the setup improvements mentioned it would also be possible to conduct a study analyzing the effects of total mass flow rate similar to what was done by DLR. Additionally, longer aging tests of three hours or more should be performed to see if the current trends hold. These two analyses could be used to greatly improve the technique and give context to or even correct new results based on the flow rate and age of the filament. It was shown in the Propagation of Errors section that the largest source of uncertainty in the gas phase temperature stems from the use of radiation correction. Two factors, the total emissivity and the heat transfer coefficient, and achieving better accuracy for both could yield a large reduction in error. The use of a Nusselt number correlation based on data that more closely mimics the current application would be an easy first step. Additionally, since literature data is available for the total emissivity of SiC versus temperature, the calculated filament temperature could be used to interpolate a value for each condition as opposed to simply using a static value. Finally, the biggest target should be to implement the technique in other flames, especially those with very different conditions. The current list of items for future work is not exhaustive and it is also only based on the challenges encountered through this application. Implementation in starkly different environments would surely lead to unexpected new challenges, further improvement and optimization, and the increased versatility of the technique in the long run.

Bibliography

Balat-Pichelin, M., & Bousquet, A. (2018). Total hemispherical emissivity of sintered SiC up to 1850 K in high vacuum and in air at different pressures. *Journal of the European Ceramic Society, 38(10), 3447–3456*. https://doi.org/10.1016/j.jeurceramsoc.2018.03.050

Bergman, T. L., Lavine, A. S., Incropera, F. P., & DeWitt, D. P. (2011). Fundamentals of Heat and Mass Transfer (7th ed.). *John Wiley & Sons, Hoboken.*

Butler, B., Shannon, K. S., & Butler, B. W. (2003). A Review of Error Associated with Thermocouple Temperature Measurement in Fire Environments. *USDA Forest Service.* https://www.researchgate.net/publication/228496160

Dunn-Rankin, D., Padilla, R. E., Minniti, M., Jaimes, D., Garman, J., & Pham, T. K. (2013). Thin filament pyrometry for temperature measurements in Fuel Hydrate flames and Non-premixed water-laden methane-air flames. *The 8th US National Combustion Meeting.*

Hunt, L. B., & Matthey, J. (1964). The Early History of the Thermocouple. *Platinum Metals Review, 1964, 8, (1) 24-28.*

Ku, H. H. (1966). Notes on the Use of Propagation of Error Formulas. *Journal of Research of the National Bureau of Standards, 1966, Vol 70C No. 4, 263-273.*

Kuhn, P. B., Ma, B., Connelly, B. C., Smooke, M. D., & Long, M. B. (2011). Soot and thin-filament pyrometry using a color digital camera. *Proceedings of the Combustion Institute, 33(1), 743–750*. https://doi.org/10.1016/j.proci.2010.05.006

Ma, B., Wang, G., Magnotti, G., Barlow, R., & Long, Marshall. (2013a). Intensity-ratio and color-ratio thin-filament pyrometry: Uncertainties and accuracy. *Combustion and Flame, 2013, 161 Issue 4, 908-916.*

Ma, B., Wang, G., Magnotti, G., Barlow, R. S., & Long, M. B. (2013b). Recent Developments of Thin-Filament Pyrometry. *8th U. S. National Combustion Meeting.*

Maun, J. D., Sunderland, P. B., & Urban, D. L. (2007). Thin-filament pyrometry with a digital still camera. *Applied Optics, 2007, Vol. 46, No. 4, 438-488.*

Sun, H., Hao, X., Wang, J., Tai, B., & Zhao, Y. (2021). Thin filament pyrometry to measurement the butane air flame combustion flame. *Proc. of SPIE Vol. 11897.* https://doi.org/10.1117/12.2599688

Vilimpoc, V., Goss, L. P., & Sarka, B. (1988). Spatial temperature-profile measurements by the thin-filament-pyrometry technique. *Optics Letters Vol. 13, Issue 2, 93-95.*

Wang, G., Bonilla, C., & Kalitan, D. (2014). Gas Temperature Field Measurement Using Thin-Filament Pyrometry. *Proceedings of ASME Turbo Expo 2014.* http://asmedigitalcollection.asme.org/GT/proceedings-pdf/GT2014/45752/V006T06A007/4234435/v006t06a007-gt2014-25909.pdf

Weigand, P., Lückerath, R., & Meier, W. (2003). Documentation of Flat Premixed Laminar CH_4 /Air Standard Flames: Temperatures and Species Concentrations. *DLR – Institute of Combustion Technology.* www.dlr.de/VT/Datenarchiv